Available online at www.sciencedirect.com

ScienceDirect

Geochimica et Cosmochimica Acta 124 (2014) 152–169

Geochimica et Cosmochimica Acta

www.elsevier.com/locate/gca

A transmission electron microscopy study of presolar spinel

Thomas J. Zega [a,b,e,*], Larry R. Nittler [c], Frank Gyngard [c,d], Conel M.O'D. Alexander [c], Rhonda M. Stroud [e], Ernst K. Zinner [d]

[a] Department of Planetary Sciences, Lunar and Planetary Laboratory, University of Arizona, 1629 E. University Blvd, Tucson, AZ 85721-0092, United States

[b] Department of Materials Science and Engineering, University of Arizona, Tucson, AZ, United States

[c] Department of Terrestrial Magnetism, Carnegie Institution of Washington, 5241 Broad Branch Rd NW, Washington, DC 20015, United States

[d] Laboratory for Space Sciences and Physics Department, Washington University, One Brookings Drive, Physics Department, Campus Box 1105, St. Louis, MO 63130, United States

[e] Materials Science and Technology Division, Naval Research Laboratory, 4555 Overlook Ave. SW, Washington, DC 20375, United States

Received 6 November 2012; accepted in revised form 9 September 2013; Available online 25 September 2013

Abstract

We report on the isotopic and microstructural properties of four presolar spinel grains identified in acid-resistant residues of the Murray CM2 and Orgueil (ORG) CI1 chondrites, and a mixture of the unequilibrated ordinary chondrites (UOC) QUE 97008 (L3.05), WSG 95300 (H3.3), and MET00452 (LL3.05) collected in Antarctica. All four grains have O-isotopic compositions indicating an origin in low-mass ($\sim$1.2–1.4 $M_{\odot}$) O-rich asymptotic giant branch (AGB) stars, although two of the grains have compositions indicating that non-standard mixing (cool-bottom processing) likely occurred in their parent stars. Three of the grains are single-crystal Mg–Al-rich spinels containing minor Fe and Cr; one is Mg deficient and one contains minor Ca. The fourth consists of an assemblage of three, Fe–Cr-rich crystalline grains with closely aligned crystallographic orientation but systematically varied cation composition. Each spinel grain within the assemblage also contains Ti-rich subgrains (<100 nm) whose lattice structures are coherent with their host crystals. Oxygen isotope measurements of the Orgueil residue identified four additional particles all with similar elemental and isotope composition. These are the first known presolar Fe–Cr-rich spinels.

The isotopic and microstructural data indicate that the Al–Mg-rich and Fe–Cr-rich grains experienced different condensation and processing histories. The single-crystal, stoichiometric, nearly pure Mg–Al spinels are generally consistent with equilibrium condensation predictions, which constrain their condensation temperatures between 1161 and 1221 K, assuming total gas pressures of 1×10^{-6} and 1×10^{-3} atm, respectively. Minor stacking disorder is observed in one of the Mg–Al spinels and is probably a result of slight perturbations to crystal growth during condensation in the circumstellar environment or of impact-induced sheer strain as a response to grain-grain collisions, which could have occurred in the circumstellar environment, the interstellar medium, or the solar nebula. The minor Ca in one of the Mg–Al spinels suggests back reaction with the circumstellar gas from which it formed. In comparison, the similarly oriented Fe–Cr-rich grains of the Orgueil assemblage and their homogeneous isotopic compositions are consistent with their condensation as a single circumstellar dust particle. However, the Fe–Cr-rich compositions (nearly chromite) are inconsistent with predictions for equilibrium condensation and suggest a complex cooling history that is not possible to precisely constrain.

* Corresponding author at: Lunar and Planetary Laboratory, Department of Planetary Sciences, University of Arizona, 1629 E. University Blvd, Tucson, AZ 85721 0092, United States. Tel.: +1 520 626 1356; fax: +1 520 621 4933.

E-mail address: tzega@lpl.arizona.edu (T.J. Zega).

0016-7037/$ - see front matter © 2013 Elsevier Ltd. All rights reserved.
http://dx.doi.org/10.1016/j.gca.2013.09.010

1. INTRODUCTION

Dust grains that condensed in the gaseous outflows of ancient stars and survived transport through the interstellar medium were incorporated into the reservoir of material that formed our solar system. These presolar stardust grains are preserved in primitive meteorites, and their chemistries and structures can provide information on the nucleosynthetic and thermodynamic histories of their parent stars. Identifying such grains and extracting them for detailed analysis is a challenging task because they are embedded in a matrix of meteoritic material that formed within our solar nebula. Dissolution of this bulk solar material greatly increases the chances of finding acid-resistant presolar phases. Such a 'burning-down-the-haystack-in-order-to-find-the-needles' approach, has led to the identification of several different types of circumstellar grains including carbides, graphite, nitrides, and oxide stardust (e.g., Bernatowicz et al., 1987; Amari et al., 1990; Nittler et al., 1997; Daulton et al., 2002; Stroud et al., 2004; Zinner, 2004; Croat et al., 2005; Stadermann et al., 2005; Zinner et al., 2005; Gyngard et al., 2010; Hynes et al., 2010; Zega et al., 2011).

The identification of presolar grains is usually based on their isotopic compositions, relative to materials that formed in the solar system. Isotopic deviations larger than can be explained by chemical or physical processes in the solar system signify a presolar, stellar nucleosynthetic origin. Thus, the isotopic compositions of presolar grains provide insights into the workings of stellar interiors and transport to the stellar surfaces where the grains condensed. Isotopic analyses, largely by secondary ion mass spectrometry (SIMS), have consequently played a prominent role in presolar-grain research over the past three decades (Zinner, 2004). However, the recognition that information on microstructures and crystal chemistry, such as that made possible by transmission electron microscopy (TEM), could provide additional information on the formation processes and transport histories of presolar materials led to the development of techniques that enable isotopic and microstructural data to be obtained from the same grains (Bernatowicz et al., 1987, 2005). The coordinated isotope-microstructural approach to presolar grain studies has continued to improve, especially with the development of the focused-ion-beam scanning-electron microscope (FIB-SEM) as a viable mineralogical tool (e.g., Stroud et al., 2000, 2004; Heaney et al., 2001; Lee et al., 2003; Zega et al., 2007; Graham et al., 2008). The FIB-SEM has extended the kinds of samples that can be analyzed and the data that can be acquired from them (Stroud et al., 2004, 2006, 2007, 2009; Nguyen et al., 2007, 2010; Vollmer et al., 2007, 2009; Zega et al., 2007, 2011; Leitner et al., 2012). Here we apply the coordinated SIMS/FIB-SEM/TEM approach to the study of presolar spinel grains. Our goal is to understand their origins within their circumstellar envelopes, and if possible, their histories after such condensation, i.e., transport histories through the ISM and alteration in meteorite parent bodies.

A number of minerals belong to the spinel group. All spinels have a face-centered cubic structure (space group Fd3m) with a generalized formula of XY_2O_4, where X = Mg, Fe, Ni, and Y = Al, Ti, and Cr. The solid-solution chemistry possible in spinel structures translates into a range of lattice constants of approximately $0.810\ \text{nm} < a_0 < 0.854\ \text{nm}$ (Deer et al., 1992). A variety of spinel-group minerals occur in extraterrestrial samples, including as components of Ca–Al-rich inclusions, amoeboid olivine aggregates (AOAs), chondrules, and the matrices of primitive meteorites (Papike, 1998 and references therein). Thermodynamic equilibrium calculations predict that $MgAl_2O_4$ (Mg–Al) spinel will condense from a gas of solar composition (Yoneda and Grossman, 1995; Lodders, 2003; Ebel, 2006), perhaps explaining its abundance in refractory inclusions and chondrite matrices. Both Mg–Al and magnesiochromite spinels have also been identified as presolar phases (Nittler et al., 1994; Choi et al., 1998, Zinner et al., 2005). Mg–Al spinel is estimated to be among the most abundant presolar-oxide phases in primitive meteorites, occurring with abundances of tens-to-hundreds of ppm, grain sizes in the hundreds of nanometers, and O-isotopic compositions that indicate origins in RGB and AGB stars (Nguyen et al., 2007). Further, the 13-μm emission feature of IR spectra of O-rich AGB stars has been attributed to several phases including spinels (Onaka et al., 1989; Kozasa and Sogawa, 1997; Posch et al., 1999; Speck et al., 2000). Thus, microstructural and crystal-chemical investigation of bona fide presolar spinel grains could aid in the identification of the materials responsible for the 13-μm feature and other features around such stars. Here we also report on the first presolar Fe–Cr-rich presolar spinels.

2. SAMPLES AND ANALYTICAL METHODS

2.1. SIMS

The presolar spinel grains that we studied for isotopic and microstructural properties were all isolated from acid-resistant residues of primitive chondritic meteorites. Two $MgAl_2O_4$ grains (UOC-S1 and UOC-S2) were previously reported from a mixed residue of three (Queen Alexandra Range, QUE 97008; Mount Wisting, WSG 95300; and Meteorite Hills, MET 00452) unequilibrated ordinary chondrites (UOC) collected in Antarctica (Nittler et al., 2008). A third analyzed $MgAl_2O_4$ grain (Murray 2-19-13, Nittler et al., 2010) was found in the same acid residue of the Murray CM chondrite reported by Zinner et al. (2003, 2005) and Gyngard et al. (2010). Isotopically anomalous Cr-bearing spinels were found in a previously reported acid residue of the Orgueil CI chondrite (Zinner et al., 2005). Aliquots of the residues were drop cast onto conductive Au foils to mitigate charge buildup under the ion beam during SIMS analysis.

Two of the $MgAl_2O_4$ grains (UOC-S1 and UOC-S2) and the Fe–Cr-rich Orgueil grain (ORG-36-21) were identified by automated O isotopic measurements performed by magnetic field switching with a custom automated analysis program for the Cameca ims-6f ion microprobe (Nittler and Alexander, 2003). Grain Murray 2–19-13 was automatically measured for $^{16}O^-$, $^{17}O^-$, $^{18}O^-$, as well as $^{24}Mg^{16}O^-$ and $^{27}AlO^-$ to estimate mineralogy, in multicollection mode with a similar analysis program developed and adapted

for the Cameca NanoSIMS (Gyngard et al., 2010). For both instruments, the automated analysis techniques are, in principle, identical. Raster ion images are acquired for each isotope over an area that is typically 10–20 μm on a side. A software algorithm then automatically defines particles in these images, and the primary beam (~100 nm and 1000 nm in diameter for the NanoSIMS and ims-6f, respectively) is electrostatically deflected to each grain so that their secondary ion ratios can then be determined. The sample stage is subsequently automatically moved to a new location and the entire process repeated; in this way, it is possible to measure over a thousand individual grains in about a week. The NanoSIMS has the advantage of higher sensitivity at highmass resolution and the capability of multi-collection compared to the ims-6f, allowing for shorter measurement times and less destruction of the grains due to primary beam sputtering.

Following their identification, the UOC presolar spinels were re-analyzed for their Mg–Al isotopic compositions with the Carnegie NanoSIMS 50L as previously reported (Nittler et al., 2008), and the presolar Cr-bearing spinels from Orgueil were reanalyzed for O^- and Mg-isotopic compositions with the Washington University NanoSIMS 50 ion probe. Oxygen measurements were made in imaging mode with a ~100 nm Cs^+ primary beam to search for isotopic heterogeneity in the grains. Images were quantitatively analyzed with the L'image software (L. Nittler, CIW). Magnesium isotopes were measured with an O^- primary beam and standard analytical techniques (Zinner et al., 2005).

2.2. FIB and TEM

We investigated the microstructure and crystal-chemistry of the three Mg–Al grains and one of the Orgueil Fe–Cr-rich grains (ORG-36-21) after SIMS analysis in order to determine their mineralogy, infer the conditions under which they formed, and investigate their interstellar and solar-system processing histories. Each grain was extracted and thinned to electron transparency (⩽100 nm) at the Naval Research Laboratory with an FEI Nova 600 FIB-SEM. We used the in situ techniques previously described by Zega et al. (2007), with the exception that the grains were welded to grids (Cu or Mo) rather than extracted with a microtweezer. We attempted to prepare three additional grains, but we were unsuccessful primarily due to their small grain sizes (≈200 nm for one of them) and/or over-aggressive ion milling.

The FIB sections of UOC-S1, UOC-S2, ORG-36-21, and Murray 2-19-13, were analyzed with a 200 keV JEOL 2200FS TEM equipped with an energy-dispersive X-ray spectrometer (EDS) and scanning TEM (STEM) bright- and high-angle annular-dark-field (HAADF) detectors. HAADF images were acquired using 80- and 175-mrad collection semi-angles, and the contrast from such images follows a $Z^{1.5}$ to Z^2 dependency, which we have confirmed previously for this microscope (Zega et al., 2006). Grain compositions were determined with an ultra-thin-window ThermoElectron Si(Li) EDS detector. Illumination conditions were adjusted to optimize counting statistics (high count rate, spectrometer dead time ⩽30%), and therefore, integration times varied between one and seven minutes. Standardless quantification of all spectra was based on a Cliff–Lorimer thin-film matrix correction and Gaussian peak fits. The accuracy of the software K factors for Mg, Al, and Fe was verified previously with San Carlos Olivine and Tanzanian hibonite standards (Zega et al., 2011). The peak fit quality was assessed via simulated spectra and analysis of the residual intensity after subtraction of the simulated spectra through the SpectraCheck feature in Noran System Six software. This allowed for assessment of the fitting of closely spaced X-ray peaks, particularly at low energies, e.g., Al and Si. The quality of the fit was further assessed based on the reduced chi-square values. Mineral stoichiometry was determined by assuming that all elements are present as oxides and that there are four O atoms per formula unit. The EDS detection limits are estimated to be ⩽0.1 wt%, with the indicated errors based on counting statistics.

Mineral structure was determined using selected-area electron diffraction (SAED) where possible. Attempts were made to acquire SAED patterns in multiple orientations, and these are shown and discussed where relevant. All diffraction patterns were measured both manually (with Adobe Photoshop) and with the Crystallographic Processing Software Package (CRISP) (Hovmöller, 1992) based on calibrated camera constants. Indexing of the SAED patterns was based on the cubic (S.G. Fd3m) spinel structure and lattice constants (see above) and verified through simulated patterns calculated with the JEMS multislice (Stadelmann, 1987) and CrystalMaker software packages.

3. RESULTS

3.1. Automated O-isotopic measurements

UOC results have been discussed in detail (Nittler et al., 2008). Six grains identified within the Orgueil residue had O-isotopic ratios significantly outside the range of solar system values and were hence identified as presolar grains. Subsequent SEM analysis revealed that one of the anomalous grains was Mg-rich Al_2O_3 and the remaining five grains were Fe- and Cr-rich with varied amounts of Mg and Al. Here we focus on the Fe–Cr-rich grains as presolar chromite has not been previously reported in the literature (though see Dauphas et al., 2010; Qin et al., 2011); the Orgueil Al_2O_3 grain was the focus of a separate study (Stroud et al., 2007). Isotopic imaging with the Washington University NanoSIMS confirmed the original ims-6f O-isotopic data for the Fe–Cr-spinels and indicated that the grains were isotopically homogeneous on a scale of a few hundred nm (see below). Three of the Orgueil grains were also analyzed for their Mg isotopic composition with the NanoSIMS.

The Murray spinel grain discussed below was found by measurements of a spinel-rich residue previously analyzed by Zinner et al. (2003). Thousands of grains with an average diameter of ~450 nm were automatically measured with the Carnegie NanoSIMS, following procedures described by Gyngard et al. (2010). A total of 107 isotopically

anomalous grains were identified, of which 37 were found to be $MgAl_2O_4$ and 8 Al_2O_3; the remainder are multiple grains for which unique mineralogical identification has not yet been possible. The total Murray dataset was initially reported by Nittler et al. (2010) and will be presented in detail elsewhere. For the present study, a presolar spinel grain (2-19-13) with an O-isotopic composition near the average value for presolar oxides was selected for detailed mineralogical analysis.

The O- and Mg-isotopic compositions of the five identified Fe–Cr-rich spinels from Orgueil and the three $MgAl_2O_4$ grains studied by TEM are given in Table 1. The O-isotopic ratios for the four grains analyzed by TEM are shown, along with other presolar oxide grains, in Fig. 1. The five Fe–Cr-rich grains have O-isotopic compositions that are remarkably similar to each other with $^{17}O/^{16}O$ ratios some 30% higher than the terrestrial value and $^{18}O/^{16}O$ ratios close to solar (Table 1). This composition places these grains in the Group-1 field for presolar oxides as originally defined by Nittler et al. (1997). Two of the three Cr-rich grains analyzed for Mg isotopes show slight depletions in the heavy Mg isotopes ^{25}Mg and ^{26}Mg (Table 1), similar to a previously reported Orgueil Mg–Cr-rich spinel grain (Zinner et al., 2005). Like the Cr-spinels, the three analyzed Mg–Al spinels are also ^{17}O-rich, but also show a range of ^{18}O depletions, relative to solar system materials. Grain UOC-S2 ($^{18}O/^{16}O$ ~25% of solar) clearly plots in the Group-2 field of highly ^{18}O-depleted grains, whereas grains UOC-S1 and Murray 2-19-13 plot close to the border of Groups 1 and 2. A detailed discussion of the O-isotopic compositions of Group-1 and -2 presolar oxide grains was previously provided by Nittler et al. (2008). The exact locations in which these grains plot in the three-O isotope space reflect their nucleosynthetic histories, and hence, the evolutionary state of the stars from which they condensed. These are discussed in more detail below.

3.2. Grain morphology

Fig. 2 shows SEM images of the five identified presolar Fe–Cr-rich grains from Orgueil. All grains sit on Au pedestals in relief from the conductive Au substrate. This geometry results from the differential sputtering of the relatively soft Au and the hard spinel material by the primary Cs^+ beam during SIMS analysis. The grains range in size from 0.8 to 4 μm and several show a blocky appearance, suggesting that they are aggregates of smaller grains. However, NanoSIMS O-isotopic imaging showed that the grains are isotopically homogenous on a scale of a few hundred nanometers (e.g., Fig. 2f). So, if the grains are indeed aggregates (as confirmed by the TEM data for ORG-36-21, see below), the sub-grains all seem to share the same O-isotopic composition.

The spinel grains chosen for TEM analysis range in size from 336 × 428 nm (UOC-S1) to 845 × 2066 nm (ORG-36-21), as measured in orthogonal directions across each grain from SEM images acquired after the SIMS analyses but prior to FIB-SEM preparation (Fig. 3). The grains exhibit both rough (Figs. 2 and 3a, b) and smooth (Figs. 2 and 3c, d) surface morphologies. We present their microstructural data below.

Table 1
Oxygen and Magnesium isotopic composition of presolar spinel grains identified in this study.

Grain	ORG-55-38	ORG-49-14	ORG-16-1	ORG-36-21	ORGCR2C-15-36	Murray 2-19-13	UOC-S1	UOC-S2
$^{17}O/^{16}O \pm 1\sigma$	$4.82 \pm 0.05 \times 10^{-4}$	$5.14 \pm 0.06 \times 10^{-4}$	$4.86 \pm 0.06 \times 10^{-4}$	$4.89 \pm 0.06 \times 10^{-4}$	$4.6 \pm 0.2 \times 10^{-4}$	$8.9 \pm 0.4 \times 10^{-4}$	$5.35 \pm 0.36 \times 10^{-4}$	$8.52 \pm 1.33 \times 10^{-4}$
$^{18}O/^{16}O \pm 1\sigma$	$2.07 \pm 0.03 \times 10^{-3}$	$2.07 \pm 0.03 \times 10^{-3}$	$2.10 \pm 0.03 \times 10^{-3}$	$2.06 \pm 0.03 \times 10^{-3}$	$1.8 \pm 0.07 \times 10^{-3}$	$1.10 \pm 0.04 \times 10^{-3}$	$1.29 \pm 0.08 \times 10^{-3}$	$5.49 \pm 1.40 \times 10^{-4}$
$\delta^{25}Mg/^{24}Mg \pm 1\sigma$	-22 ± 5	n.m.	-11 ± 4	-1 ± 4	n.m.	n.m.	-4 ± 11	256 ± 10
$\delta^{26}Mg/^{24}Mg \pm 1\sigma$	-28 ± 8	n.m.	-27 ± 8	-12 ± 8	n.m.	n.m.	241 ± 14	1020 ± 17
$^{26}Al/^{27}Al \pm 1\sigma$	…	…	…	…	…	…	$1.18 \pm 0.07 \times 10^{-2}$	$4.8 \pm 0.3 \times 10^{-2}$
Group	1	1	1	1	1	2	1	2
Mass ($M_\odot$)	<1.2	<1.2	<1.2	<1.2	<1.2	<1.4	1.4	<1.4
Metallicity ($Z_\odot$)	1	1	1	1	1	…	0.8	…

ORG = Orgueil; UOC = grains identified from a residue of a mixture of unequilibrated ordinary chondrites.
δ = [Rsample/Rstandard − 1] × 1000, where R is the ratio of heavy to lighter isotope.
n.m. = Not measured.
… = Cannot be inferred.

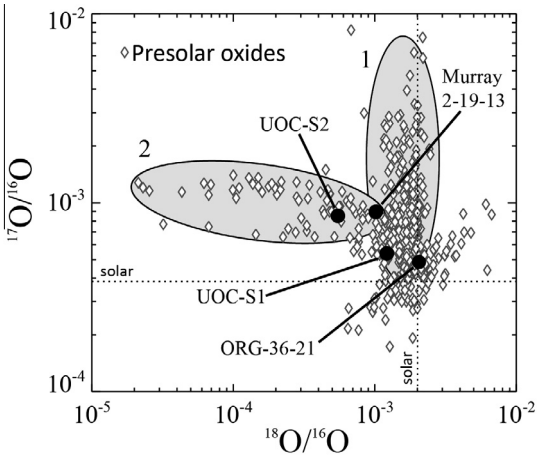

Fig. 1. Oxygen 3-isotope plot of the presolar spinel grains analyzed here by TEM (black circles) shown along with other presolar oxides (mostly Al_2O_3 grains). The ellipses (gray ovals) represent the broad groups into which these and other presolar oxide grains have been divided (see Nittler et al., 2008 for a detailed description). The dashed lines indicate terrestrial O-isotopic composition.

3.3. TEM results

3.3.1. Murray 2-19-13

Bright-field (BF) and HAADF STEM imaging of the FIB cross-section of Group-2 Mg–Al grain Murray 2-19-13 reveals that in fact it is composed of three grains, one of which is nearly surrounded with Au due to re-deposition either during SIMS analysis or FIB preparation (Fig. 4a, b). The three SAED patterns (Fig. 4c–e) acquired from two of the grains (Fig. 4a) are consistent with Mg–Al spinel, and EDS measurements show quantitative agreement with spinel stoichiometry (Table 2). EDS measurements indicate that the third grain (black arrowhead, Fig. 4a) is SiC. The original NanoSIMS measurement was from the top of the section. Thus, of the two spinels, the grain at the lower left ('c' in Fig. 4a) was shielded from the SIMS analysis and the grain on the right-hand side ('e' &'d', Fig. 4a) must be the isotopically anomalous presolar grain. The other spinel ('c') occurs below the SiC in the FIB section, and its isotopic composition was thus not measured. However, because presolar grains make up only a small fraction of meteoritic spinel grains, this grain is most likely of solar system origin. We acquired SAED patterns from two separate areas of the presolar spinel grain to verify its crystallinity; each was acquired at the same orientation (see tilt angles indicated in Fig. 4d, e) and each indexed to the same zone axis, indicating that the grain is a single crystal.

The presolar spinel grain measures 330 nm (height) by 518 nm (width). HAADF imaging reveals uniform contrast over the grain's area, indicating a homogeneous composition (Fig. 4b). There are areas of mottled contrast, but we attribute this to re-deposition of Pt from the strap used to protect the section during thinning in the FIB-SEM and/or re-deposition of sputtered Au from the underlying foil. Quantification of its EDS spectrum gives $(Mg_{0.97}Fe_{0.02})$

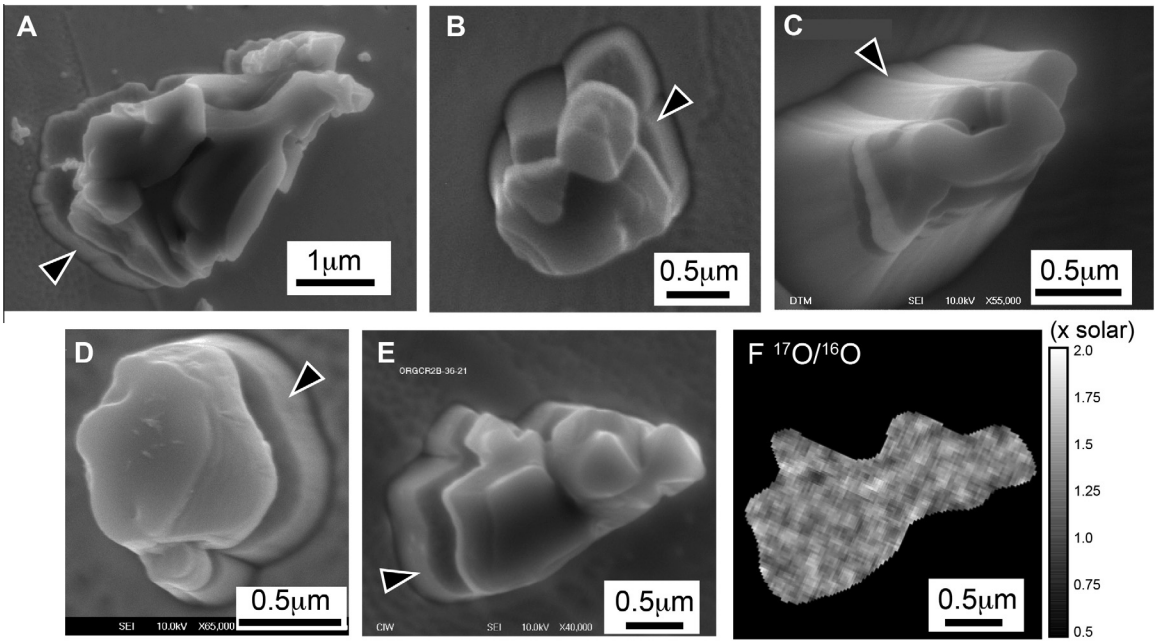

Fig. 2. Secondary electron and O-isotopic images of the five presolar Fe–Cr-rich spinel grains found in an Orgueil acid residue (Table 1). Each grain occurs on a Au pedestal (black arrowhead with white outline), produced as a result of the different sputtering rates of the oxide grain and the Au, the latter which is used as a conductive substrate for the SIMS analysis. (a) ORG-16-1, (b) ORG-55-38, (c) ORG-15-36, (d) ORG-49-14, (e) ORG-36-21 (f) NanoSIMS $^{17}O/^{16}O$ image of grain ORG-36-21; the grain is homogeneously enriched in ^{17}O by ≈30% on a few hundred-nm scale; apparent variations are within statistical uncertainties.

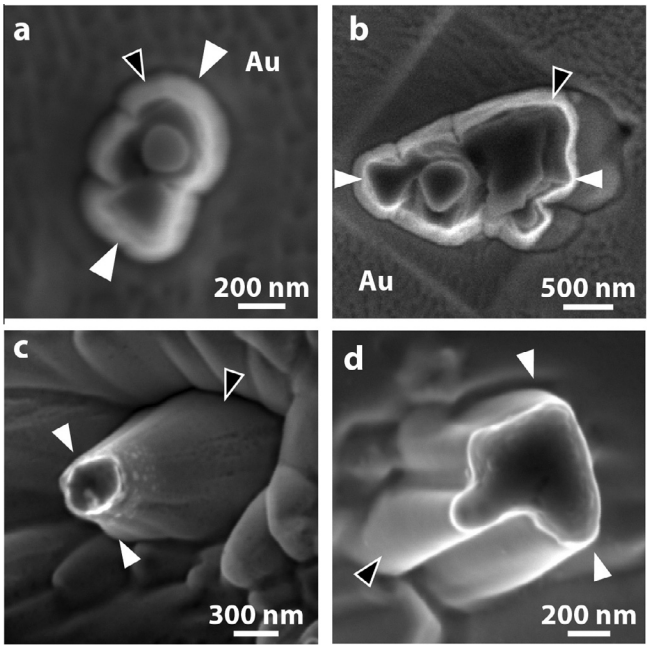

Fig. 3. Secondary electron images of the four presolar-spinel grains analyzed by TEM, prior to FIB sectioning. (a) Murray 2-19-13, (b) ORG-36-21, (c) UOC-S1, and (d) UOC-S2. Each grain occurs on a Au pedestal (black arrowhead with white outline), produced as a result of the different sputtering rates of the oxide grain and the Au, the latter which is used as a conductive substrate for the SIMS analysis. The lines along which the protective Pt straps were deposited for each of the grains (to mitigate ion implantation and radiation damage), and hence, the locations of the FIB section, are indicated by the white arrowheads.

$(Al_{1.74}Cr_{0.22}Si_{0.03})O_4$ (Table 2). The contrast in the HAADF image of the adjacent probably solar spinel grain is also uniform, suggesting that it too has a homogeneous composition. We note, however, that the contrast of the spinel in the lower-left part of the assemblage is also darker than that of the presolar spinel grain (Fig. 4b), suggesting it has, on average, a lower atomic number. Quantification of the X-ray spectrum from the solar spinel (black circle, Fig. 4a) yields $(Mg_{0.97}Fe_{0.005})(Al_{2.01}Cr_{0.009})O_4$ (Table 2). The presolar spinel is Cr-rich and Al-poor relative to the solar spinel, and the chemistry and HAADF contrast are consistent with the differences in average atomic number of the two grains.

3.3.2. UOC-S1

Bright-field and HAADF STEM imaging show that the Group-1 grain UOC-S1 is approximately 173 × 395 nm as measured in orthogonal directions (Fig. 5). SAED patterns acquired across the grain show that it is a single-crystal spinel (Fig. 5c–e). Bright-field imaging reveals a mottled contrast throughout the grain (Fig. 5a). The HAADF image intensity also varies across the grain (Fig. 5b), but this is due to re-deposition of Pt from the strap and/or re-deposition of Au from the underlying foil. The circular intensity rings in the SAED patterns (Fig. 5c–d) are consistent with diffraction from Pt and/or Au nanoparticles. Areas of the spinel grain that are free of metal re-deposition appear to be uniform in HAADF intensity, indicating a homogeneous composition. EDS shows that the grain is non-stoichiometric, with an average formula of $(Mg_{0.68}Fe_{0.03}Ca_{0.01})(Al_{2.19}Cr_{0.01})O_4$ (Table 2). The prior SIMS measurement of this grain (Nittler et al., 2008) indicated an Al/Mg molar ratio of 2.2, significantly lower than the EDS value of approximately 3.2. As discussed in detail by Gyngard et al. (2010), SIMS quantification of Al/Mg ratios in small grains may be subject to several systematic uncertainties, and the discrepancy between the TEM-EDS and the SIMS results for this grain likely reflects such an instrumental bias.

3.3.3. UOC-S2

The Group-2 $MgAl_2O_4$ grain UOC-S2 is approximately 146 × 420 nm across (Fig. 6a, b). Bright-field imaging of the grain shows that it contains mottled contrast throughout (Fig. 6a), probably due to Pt and/or Au re-deposition during FIB milling. SAED patterns acquired across the grain show that it is a single-crystal spinel (Fig. 6c–e). We observe small variations in the intensity of reflections acquired from [1 1 0] zone-axis patterns (cf., Fig. 6c–e), and discuss the possible implications of these variations below. The top-most surface of the grain lacks long-range order, and this region correlates with low-Z contrast in the HAADF image (Fig. 6b). We suspect that the disorder resulted from ion damage by the SIMS measurements, and that the lower-Z contrast, relative to the bulk spinel crystal, may be due to ^{16}O implanted from the primary beam during the measurements of Mg and Al isotopes (the thickness of this layer, ~50 nm, is similar to the expected implantation depth for O ions). High-resolution TEM

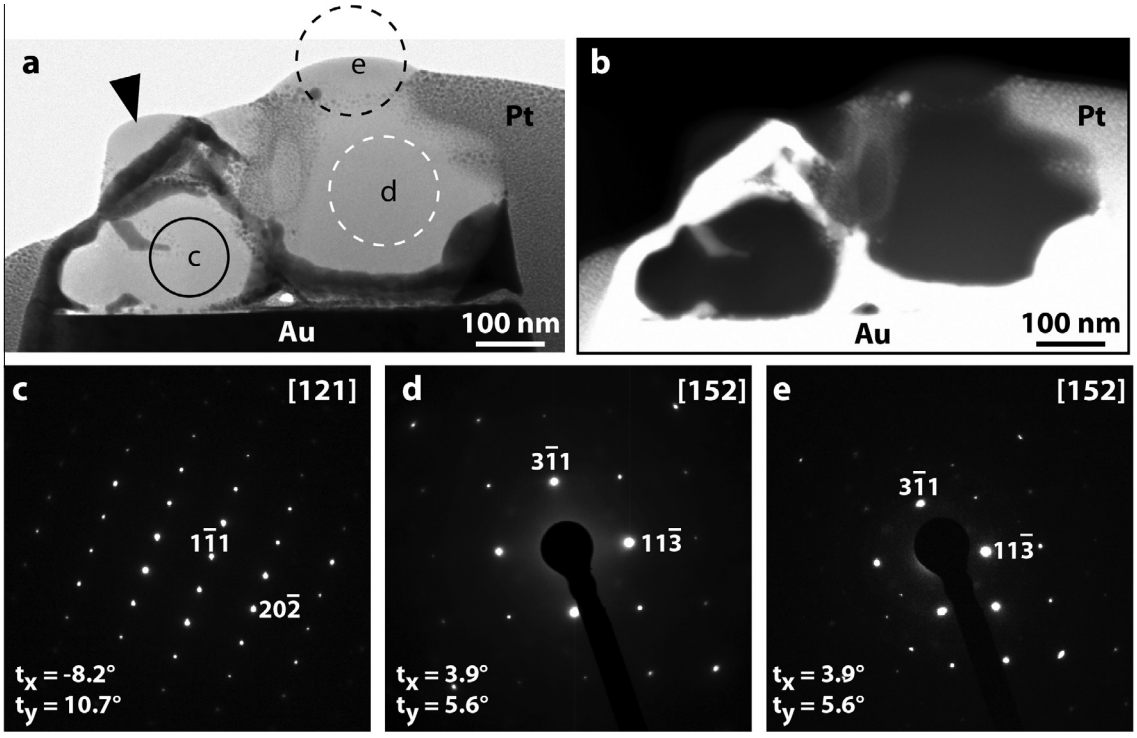

Fig. 4. TEM data for grain Murray 2-19-13. Three separate grains form a composite assemblage (cf., Fig. 3a). Two of the grains are spinel (white-dashed and solid-black circles), whereas the other is SiC (black arrowhead). The spinel grain on the right (white-dashed circle) is unambiguously the presolar grain (see text for discussion). The (probably solar) spinel grain on the left (black-solid circle) is nearly surrounded by Au due to re-deposition either during SIMS analysis or FIB preparation. (a) Bright-field STEM image, (b) HAADF STEM image, (c) SAED pattern acquired from lower-left grain in (a) indicated by the solid-black circle, (d) SAED pattern acquired from the right-hand grain in (a) indicated by the dashed-white circle, (e) SAED pattern acquired from the right-hand grain in (a) indicated by the dashed-black circle. The black object running from the lower-right corner to the center of the SAED patterns (d, e) is the beam stop to prevent over exposure of the CCD camera. The tilt angles of the TEM goniometer (t_x is about the sample-rod axis; t_y is perpendicular to it) are indicated. The SAED patterns for the presolar-spinel grain was acquired at the same orientation and both index to the same zone axis, indicating that the grain is a single crystal.

Table 2
Grain composition measured with TEM-EDS and expressed in terms of wt% oxide and cation count.

Grain	Murray 2-19-13*	Murray 2-19-13	ORG-36-21(L)	ORG-36-21(C)	ORG-36-21(R)	ORG-36-21(S)	UOC-S1	UOC-S2
MgO	26.31 (0.12)	27.32 (0.15)	6.08 (0.37)	7.75 (0.08)	7.9 (0.11)	8.09 (0.10)	19.22 (0.15)	27.35 (0.13)
Al_2O_3	59.98 (0.15)	71.93 (0.19)	3.63 (0.34)	5.7 (0.07)	6.37 (0.08)	8.08 (0.07)	78.58 (0.21)	68.73 (0.19)
CaO	n.d.	n.d.	n.d.	n.d.	n.d.	n.d.	0.26 (0.02)	n.d.
SiO_2	1.27 (0.03)	n.d.	n.d.	n.d.	n.d.	n.d.	n.d.	n.d.
TiO_2	n.d.	n.d.	4.14 (0.21)	4.61 (0.05)	6.54 (0.04)	10.95 (0.05)	n.d.	n.d.
Cr_2O_3	11.38 (0.07)	0.5 (0.02)	62.3 (0.79)	58.25 (0.14)	54.18 (0.10)	47.59 (0.11)	0.25 (0.03)	3.28 (0.04)
FeO	1.06 (0.05)	0.25 (0.03)	23.85 (0.78)	22.68 (0.09)	23.63 (0.08)	23.82 (0.10)	1.69 (0.07)	0.65 (0.03)
NiO	n.d.	n.d.	n.d.	1.00 (0.06)	1.39 (0.04)	1.48 (0.05)	n.d.	n.d.
Cations based on 4 O atoms								
Mg	0.97	0.97	0.31	0.39	0.40	0.40	0.68	0.98
Al	1.74	2.01	0.15	0.23	0.25	0.32	2.19	1.94
Ca	n.d.	n.d.	n.d.	n.d.	n.d.	n.d.	0.01	n.d.
Si	0.03	n.d.	n.d.	n.d.	n.d.	n.d.	n.d.	n.d.
Ti	n.d.	n.d.	0.11	0.12	0.17	0.27	n.d.	n.d.
Cr	0.22	0.01	1.71	1.57	1.45	1.25	0.01	0.06
Fe	0.02	0.01	0.69	0.65	0.67	0.66	0.03	0.01
Ni	n.d.	n.d.	n.d.	0.03	0.04	0.04	n.d.	n.d.

n.d. = Not detected.
L, C, R = left, center, and right spinel grains in ORG-36-21 assemblage (see Fig. 4); S = average composition of sub-grains; wt% error shown in parentheses.
* Presolar grain (see text).

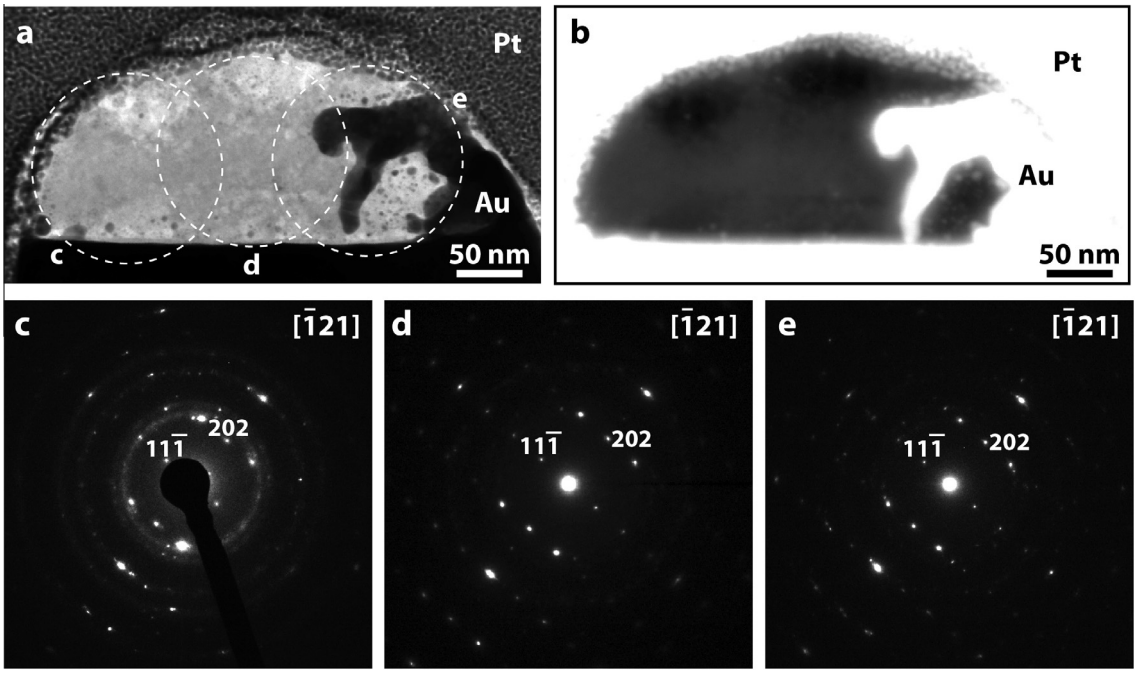

Fig. 5. TEM data on presolar spinel grain UOC-S1. (a) Bright-field STEM image, (b) HAADF STEM image, (c–e) SAED patterns acquired from regions across the grain as indicated by white-dashed circles and labels in (a), which represent the size of the smallest SAED aperture available in the TEM we used. The gray levels in (b) were adjusted to enhance the Z-contrast of the grain; otherwise it would be obscured by the saturated signal of the heavy Au and Pt. The dark and bright patch on the right-hand side of the grain in (a) and (b), respectively, is Au that was re-deposited during the FIB milling process. The circular intensity and extra reflections in the SAED patterns (c) and (e) emanate from the Pt and Au surrounding the grain, cf., the white-dashed circles in (a).

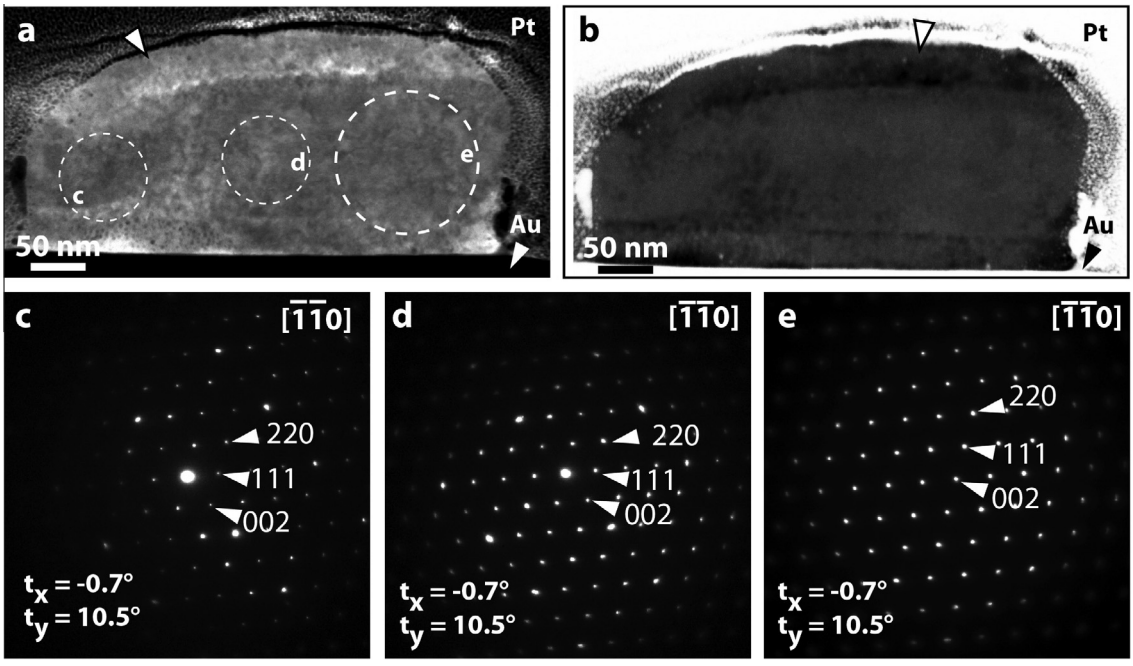

Fig. 6. TEM data on presolar spinel grain UOC-S2. (a) Bright-field STEM image, (b) HAADF STEM image, (c–e) SAED patterns acquired from areas indicated by white-dashed circles in (a). The grain contains an amorphous surface layer (white arrowhead with black outline in a and b) due to the SIMS analyses. The right-hand side of the crystal was oriented down the [1 1 0] zone axis (see the circle labeled 'e' in a), and the patterns from the middle and left-hand side of the grain ('d' and 'c', respectively, also in a) were acquired at the same goniometer tilt angles (t_x, t_y, inset).

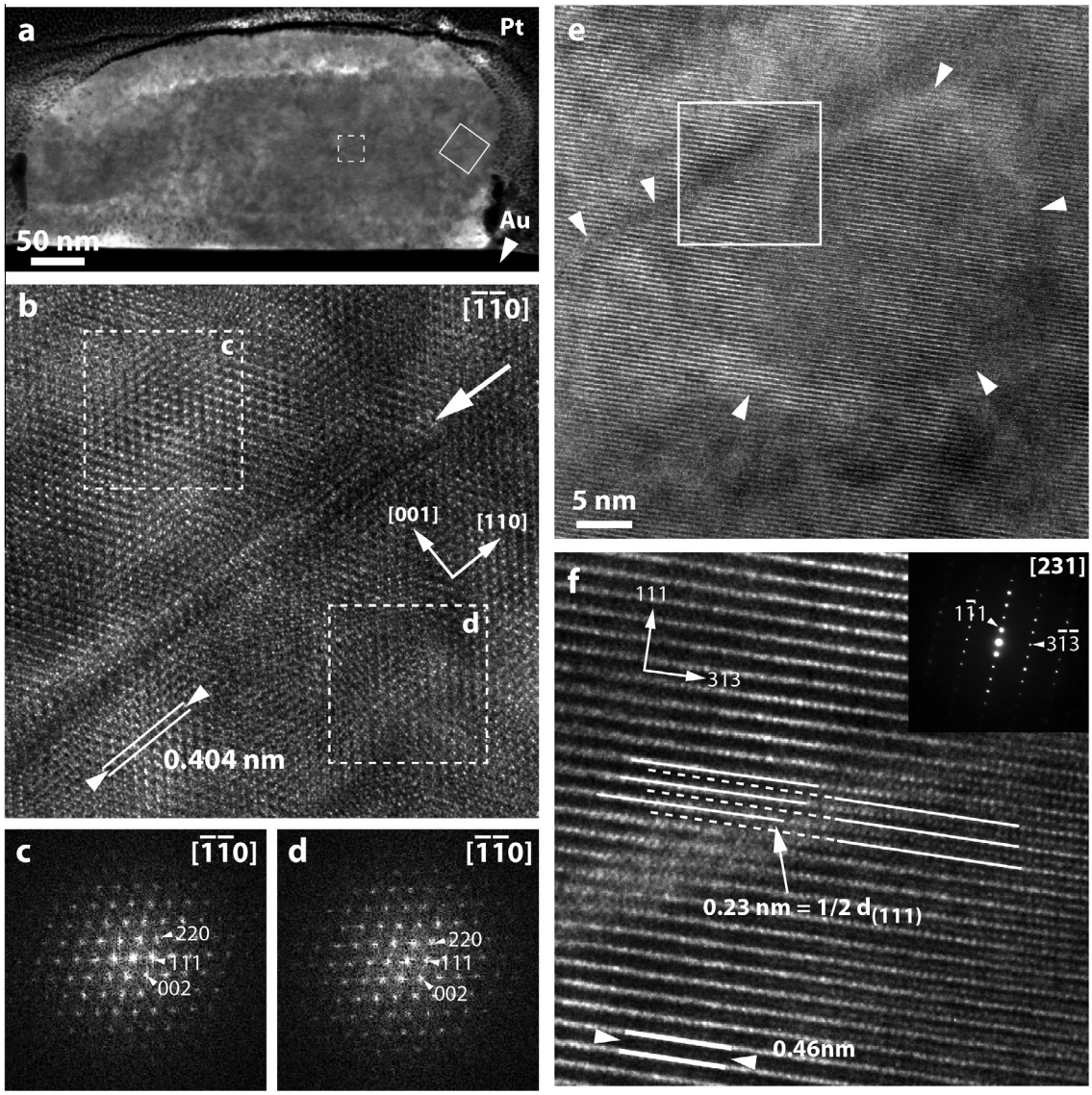

Fig. 7. TEM data on structural perturbations observed in UOC-S2. (a) Bright-field STEM image revealing local stacking disorder (white boxes) (b) HRTEM image from area outlined by the solid box in (a) acquired down the [$\bar{1}$ $\bar{1}$ 0] zone axis. A stacking fault (large white arrow) trends diagonally from the upper-right to lower-left part of the image. (c, d) Fourier transforms of the areas indicated by white-dashed boxes in (b). The transforms were acquired on opposite sides of the fault, are identical, and indicate that there is no orientation change in the local structure across the fault. (e) HRTEM image of dashed white box in (a) showing local disorder consisting of an approximately 25-nm wide loop (indicated by white arrowheads). (f) HRTEM image of area outlined by the white box in (e) acquired down the [2 3 1] zone axis (SAED inset) showing local disruption by 0.23 nm or ½ of the (1 1 1) *d*-spacing.

(HRTEM) shows that minor stacking disorder occurs in localized areas within the grain (Fig. 7). A planar stacking fault, approximately 25 nm in length, occurs on the right-hand side of the grain (cf., Fig. 7a, b), but shows no change in orientation across the fault (cf., Fig. 7b–d). HRTEM also reveals an area closer to the middle of the grain that contains an approximately 28 nm wide loop within which long-range order is locally disrupted (Fig. 7e). Measurements of the lattice fringes indicate ½(1 1 1) displacement (cf., Fig. 7a, e, f). EDS analysis of the grain yields $(Mg_{0.98}Fe_{0.01})(Al_{1.94}Cr_{0.06})O_4$ (Table 2), a stoichiometric spinel composition.

3.3.4. ORG-36-21

Bright-field and HAADF imaging reveal that the Group-1 Fe- and Cr-rich grain ORG-36-21 is a composite assemblage (Fig. 8a, b). SAED patterns (Fig. 8c–e) indicate that it is composed of three grains (black arrowheads with white outlines, Fig. 8a, b), all of which are crystalline and index to the spinel structure. The grain sizes are approximately 428 × 411, 963 × 865, and 1,300 × 876 nm for the left, center, and right-hand grains, respectively (Fig. 8a, b). The crystallographic orientations of grains c, d, and e are all within 1.5° of each other based on the goniometer tilts required to bring

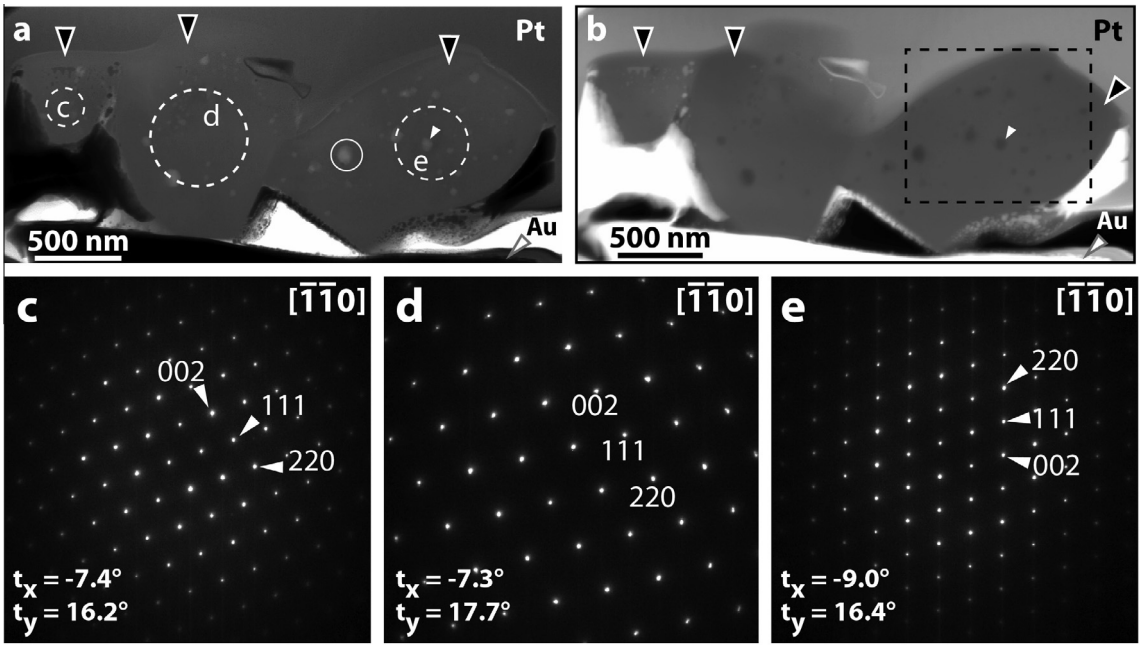

Fig. 8. TEM data on presolar spinel grain ORG-36-21. (a) Bright-field STEM image, (b) HAADF STEM image (the black rectangle is referred to in the caption for Fig. 9c), (c–e) SAED patterns acquired from areas outlined by the labeled circles shown in (a). The assemblage consists of three grains (a, b black arrowheads with white outline) sandwiched between the protective Pt strap and Au substrate (indicated). Sub-grains, which appear bright in the bright-field-STEM image and dark in the HAADF image (a, b white arrowheads) occur throughout each of the spinel crystals.

each grain onto the same [1 1 0] zone axis (Fig. 8c–e, inset).

Bright-field images of the three grains have non-uniform contrast, each containing small regions of relatively bright areas (Fig. 8a, white arrowhead) that occur heterogeneously throughout the crystals. HAADF imaging shows that these regions have, on average, lower atomic numbers than the host spinels (Fig. 8b). The low-Z regions range in width from approximately 6–94 nm with an average width of approximately 27 nm. SAED patterns and high-resolution TEM images suggest that these areas are crystalline and structurally coherent with the host spinel crystals (Fig. 9a, b), and therefore we infer that they are sub-grains with elemental compositions that are lower in average Z than the hosts. Bright-field imaging in a two-beam condition indicates that the sub-grains are euhedral and have a rhombic morphology in at least one orientation (Fig. 9c, white arrowheads).

EDS shows that the host spinel grains and the sub-grains contain Fe, Cr, Ti, Ni, Mg, Al, and O (Table 2). Quantification of the EDS spectra shows that the host spinel grains are Cr- and Fe-rich, with an average composition of $(Fe_{0.67}Mg_{0.31}Ni_{0.02})(Cr_{1.58}Al_{0.21}Mg_{0.06}Ti_{0.13})O_4$. The three host grains have a similar composition to one another as reflected in their major-element chemistry, i.e., Cr and Fe are within 10% relative (1σ), whereas the minor elements show more variability, e.g., Ni is detected in the right and center grains but not in the left grain (cf., Table 2 and Fig. 8a). We quantified spectra from several of the largest sub-grains (~90 nm) to limit spurious X-rays originating in the surrounding host material from confusing the analyses. EDS shows that the sub-grains are also Cr-rich, but quantification indicates that, on average, they contain 50% more Al, 109% more Ti, and 21% less Cr than their hosts. Quantification of spectra from the sub-grains gives an average formula of $(Fe_{0.66}Mg_{0.30}Ni_{0.04})(Cr_{1.25}Al_{0.32}Mg_{0.10}Ti_{0.27})O_4$. On average, the effective atomic number for the sub-grains ($Z_{effective} = 63$) relative to that of the bulk spinel ($Z_{effective} = 66$) is consistent with their darker contrast in the HAADF image.

4. DISCUSSION

4.1. Stellar origins

The isotopic compositions of the presolar oxide grains reflect the formation and evolutionary histories of the parent stars around which they condensed. The ^{18}O-depleted, ^{17}O-enriched trend of the Group-1 grains (Fig. 1) most likely reflects the first and second dredge-ups that occur in low- and intermediate-mass stars following core H-burning. In these dredge-up episodes, material processed by partial H-burning is mixed to the surface layers, enriching them with the products of CNO-cycle nucleosynthesis, including ^{13}C, ^{14}N and ^{17}O. The Group-1 O-isotopic ratios can be accurately reproduced by theoretical models for the first and second dredge-ups in low-mass (1.2 to 2.5 $M_\odot$) stars on the red giant (RGB) or asymptotic giant branches (AGB) of stellar evolution, respectively (Dearborn, 1992; Nittler et al., 1997; Boothroyd and Sackmann, 1999).

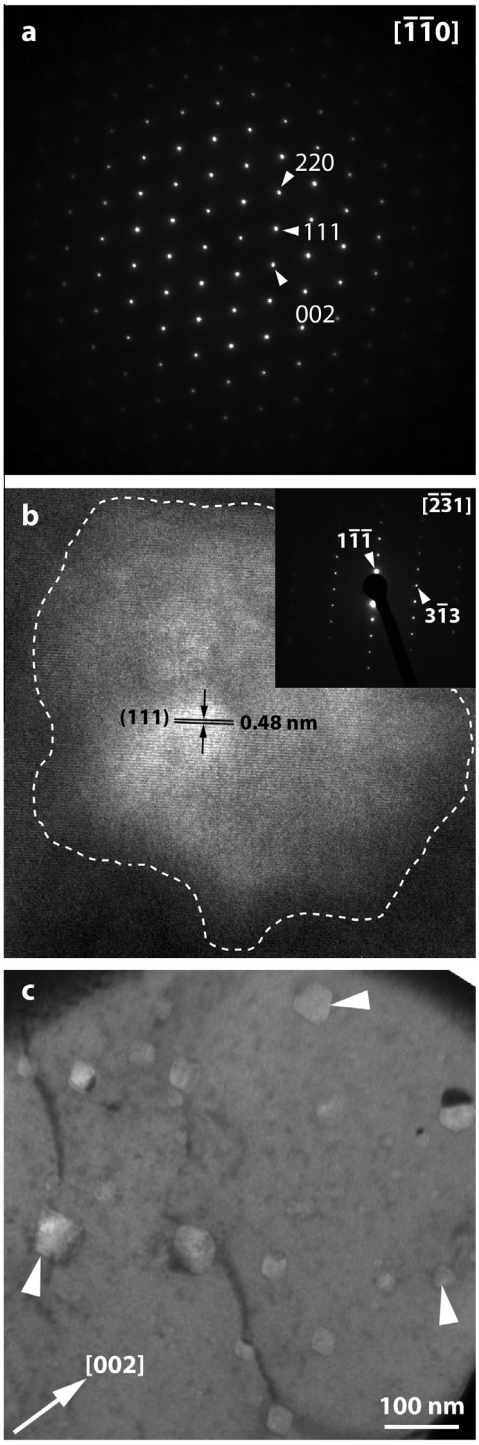

Fig. 9. TEM image data on one of the sub-grains of ORG-36-21. (a) SAED pattern acquired from the sub-grain indicated by the solid white circle in Fig. 8a. The pattern was acquired in an orientation identical to that shown in Fig. 8e and indexes to a [1̄ 1̄ 0] zone-axis pattern identical to those shown in Fig. 8c-e. (b) High-resolution image in the [2̄ 3̄ 1] orientation revealing contiguous (1 1 1) lattice fringes (indicated) across the boundary between the sub-grain and the bulk spinel crystal (white dashed line). (c) Bright-field (two-beam) image [g(0 0 2)] of the sub-grains acquired from the right-most spinel crystal (outlined by the black dashed rectangle shown in Fig. 8b). The sub-grains (white arrowheads) exhibit a euhedral rhombic morphology.

The predicted $^{17}O/^{16}O$ ratio of a star depends strongly on the stellar mass, whereas the $^{18}O/^{16}O$ ratio is more sensitive to the star's initial composition (and hence metallicity, Z). The O-isotope ratios can thus be used to estimate the stellar mass (relative to solar, $M_\odot$ and the initial metallicity, respectively, albeit in a model-dependent way (Nittler et al., 2008). For example, the O-isotopic composition of grain UOC-S1 (Table 1, Fig. 1) suggests that it formed around a low-mass ($\approx$1.4 $M_\odot$) AGB star with a metallicity of approximately 0.8 $Z_\odot$. Note that more recent first dredge-up calculations using updated CNO-cycle nuclear-reaction rates suggest a slightly lower initial mass (1.2–1.3 $M_\odot$, Palmerini et al., 2011) for its parent star. Its Mg-isotopic composition ($\delta^{25}Mg = -4 \pm 11‰$, $\delta^{26}Mg = 241 \pm 14‰$) is also consistent with this origin, with an initial $^{26}Al/^{27}Al$ ratio, inferred from the measured ^{26}Mg excess, of order 10^{-2}.

In comparison, the five Orgueil Fe- and Cr-rich spinels reported here, including ORG-36-21 for which TEM data were obtained, have $^{18}O/^{16}O$ ratios that are close to solar (Table 1, Fig. 1) and are moderately enriched (by ~30%) in ^{17}O. Comparison of the Group 1 compositions with models (Boothroyd and Sackmann, 1999; Palmerini et al., 2011) suggests an origin in low-mass (<1.2 $M_\odot$) RGB or AGB stars of approximately solar or slightly higher metallicity. Two of the Orgueil spinels have slight Mg-isotope anomalies, providing further evidence that these grains are indeed presolar circumstellar condensates, though the Mg-isotopic composition of ORG-36-21 is solar within ~1% error. The close similarity of the O-isotopic compositions (Table 1) of the five Orgueil grains stands in stark contrast to the enormous range of O-isotopic ratios observed in other presolar oxide grains and suggests one of two possibilities: (1) these five grains formed in a single star and were injected into our solar nebula; or (2) they formed in multiple stars but there is an extremely narrow range of mass and of metallicity AGB stars where micron-sized chromite grains can form. Given the O-isotope distribution of the 1300 oxide grains measured thus far (e.g., Zinner et al., 2003; Nittler et al., 1994, 2005, 2008; Hynes and Gyngard, 2009; http://presolar.wustl.edu/PGD/Presolar_Grain_Database.html) and that calculations indicate multiple stellar sources for the range of isotopic compositions exhibited by SiC (Alexander, 1993), the similar O-isotopic composition of these grains favors an origin around a single AGB star.

The large ^{18}O depletions of Group-2 oxide grains are believed to reflect extra mixing or 'cool-bottom processing' (Wasserburg et al., 1995; Nollet et al., 2003; Nittler et al., 2008; Palmerini et al., 2011) in which RGB and AGB stars may cycle envelope material through hotter regions near their H-burning shells, where ^{18}O is destroyed via $^{18}O(p,\alpha)^{15}N$. Cool-bottom processing has been invoked to explain chemical and isotopic peculiarities observed in both RGB and AGB stars, though the physical mechanism(s) responsible for the mixing remain unclear. Suggested mechanisms include rotation-induced mixing, thermohaline diffusion, and magnetic buoyancy effects (Palmerini et al., 2011 and references therein). Comparison of the O-isotopic compositions of grains UOC-S2 and Murray 2-19-13 with the results of model calculations suggests that these grains

formed in low-mass (<1.4 $M_\odot$) AGB stars (cool-bottom processing in RGB stars cannot explain the observed ^{18}O depletions, Nollet et al., 2003; Palmerini et al., 2011). Whereas the initial metallicity of Group-1 grain parent stars can be estimated from their $^{18}O/^{16}O$ ratios, this is not possible for Group-2 grains due to the strong destruction of ^{18}O during cool-bottom processing.

4.2. Microstructure and crystal chemistry

Although the isotopic data of the four grains examined by TEM indicates formation in the stellar winds of low-mass O-rich RGB and AGB stars, the TEM data show that the grains have significant differences in terms of microstructure and crystal chemistry.

The TEM data for Murray 2-19-13 reveal an assemblage composed of two spinels and one SiC. Given that all SiC grains identified in primitive meteorites appear to be presolar, this particular grain likely also condensed in a circumstellar environment (the Murray CG residue contains presolar SiC, Zinner et al., 2003). However, its proximity to the Murray grain is most likely the accidental result of drop casting the acid residue onto the conductive Au substrate during sample preparation prior to SIMS analysis. Any appearance of the grains being connected or attached (Fig. 4) is probably an amorphization artifact of SIMS analysis or FIB sample preparation, rather than being due to a genetic relationship.

As discussed earlier, the spinel grain on the left-hand side of the assemblage (Fig. 4, solid black circle) is most likely of solar system origin. Similar to the SiC grain, the spatial association of the solar and presolar spinel is a result of sample preparation. Nonetheless, it is interesting to note the differences between it and the bona fide presolar grain (cf., Fig. 4, areas indicated by black-dashed and white-dashed circles). Both grains are single crystals and both contain Fe and Cr although at very different concentrations (Table 2).

Equilibrium thermodynamic calculations show that spinel ($MgAl_2O_4$) should condense from a gas of solar composition, but that its composition should vary with condensation temperature (Yoneda and Grossman, 1995; Ebel, 2006). At high temperature, nearly pure $MgAl_2O_4$ is predicted to condense, but additional cations are expected to be included with decreasing condensation temperature. For example, nearly pure $MgAl_2O_4$ will condense at 1500 K ($P_t = 10^{-3}$ atm), but a spinel solid solution much richer in Cr is predicted to begin condensing at 1221 K at the expense of Cr-bearing metal, plagioclase, and Mg-silicates (Yoneda and Grossman, 1995).

The presolar Murray 2-19-13 spinel contains elevated Cr and Fe (Table 2), suggesting that this spinel condensed at a relatively lower temperature than the high-temperature pure Mg–Al form. The total pressure assumed in the above condensation calculations is higher than might be expected for a stellar outflow. For example, the pressure in the photospheric region of C stars is expected to range from 10^{-3} to 10^{-5} bars (1 bar = 0.9869 atm) and decrease with radial distance in the envelope (Lodders and Fegley, 1995). Moreover, lower total pressures ($P_t < 10^{-3}$ atm) lead to lower condensation temperatures. Thus, 1221 K might be considered as an upper limit for the stability of Cr-bearing Mg–Al spinel. In comparison, the presumed solar spinel (Fig. 4, black circle) contains much less Fe and Cr (Table 2) and is nearly pure Mg–Al spinel. Comparison with equilibrium predictions would constrain the condensation temperature of the solar spinel grain to 1286 and 1501 K assuming corresponding total gas pressure of 10^{-6} and 10^{-3} atm.

Whether or not there is any statistical difference between the condensation conditions for presolar and solar spinel is difficult to determine given the limited number of presolar spinel grains that have been measured for crystal structure and chemistry. Zinner et al. (2005) reported Mg (and for some grains Cr) isotopic data for 30 presolar spinel grains, 28 $MgAl_2O_4$ grains and two grains with compositions close to 1:1 mixtures of $MgAl_2O_4$ and $MgCr_2O_4$ (magnesiochromite). The SIMS data suggested non-stoichiometric Al/Mg ratios for several of the grains, but as discussed earlier, some of these results may reflect instrumental artifacts (e.g., Gyngard et al., 2010). Nonetheless, if equilibrium thermodynamics can be assumed to apply to the formation conditions of some of these grains, then higher condensation temperatures, similar to those described above for the presumed solar grain in the Murray 2-19-13 FIB section, would be implied. In comparison, we note that low petrologic type-3 chondrites, which are among the most pristine meteorites, contain abundant spinel in type-A calcium-aluminum-rich inclusions (CAIs), which are believed to be some of the first solids to have condensed in the solar nebula (MacPherson, 2004, and references therein). Most of these spinels are nearly pure $MgAl_2O_4$, but some can contain varied amounts of other metal oxides (e.g., Ti, Cr, V, Fe, Ca, Zn) in solid solution (Brearley and Jones, 1998). The impurity abundance appears to be low ($\leqslant$1 wt.%) for most grains, but some spinel in fluffy type-A CAIs (see MacPherson, 2004 for a discussion of CAI types), which are believed to be among the most primitive inclusions, can contain several weight percent Fe and Ti (e.g., MacPherson and Grossman, 1984 and Table 5 in Brearley and Jones, 1998). The limited data set on presolar spinel grains would seem to imply that their mostly pure compositions are similar to those reported for spinel grains that condensed in the early solar nebula, and that the Fe–Cr-rich presolar spinel grains (Table 2) described here are outliers. Nonetheless, additional measurements of presolar spinel grains are required to determine whether there is any statistical difference in the pressure and temperature conditions of condensation recorded by spinel in AGB star outflows versus those in the early solar nebula.

Although the SAED patterns for Group-1 grain UOC-S1 reveal that it is a single crystal spinel, the EDS measurements suggest that it is non-stoichiometric, which points to non-equilibrium condensation or incomplete back reaction with circumstellar gas. As noted above, non-stoichiometric presolar spinels were previously reported by Zinner et al. (2005) based on SIMS measurements. Those with higher than stoichiometric Al/Mg ratios were hypothesized to have formed at high temperatures by replacement of corundum (Zinner et al., 2005). While the Al/Mg ratio of UOC-S1 is, on average, higher than that expected for

stoichiometric spinel, the EDS data (Table 1) show that this grain contains minor Ca. Under equilibrium conditions, hibonite ($CaAl_{12}O_{19}$) is expected to form at much higher temperature ($T_c = 1743$ K at $T_p = 10^{-3}$ atm) than spinel, and its reaction with the residual gas (at 1500 K) is expected to be a pathway by which Mg–Al spinel is formed (Yoneda and Grossman, 1995; Ebel and Grossman, 2000; Ebel, 2006). If we assume that this spinel-forming pathway holds in the case of UOC-S1, then the presence of residual Ca might argue against the replacement of corundum and instead be the result of incomplete back reaction between hibonite and the circumstellar gas from which UOC-S1 condensed. Examination of additional non-stoichiometric spinel grains should reveal whether or not the presence of Ca is a general feature and, therefore, help test the back-reaction hypothesis. Nonetheless, as kinetic models for the spinel-hibonite transformation in circumstellar condensation environments are to our knowledge unavailable, quantitative constraints on the formation conditions for UOC-S1 cannot be inferred. However, given that the SAED data for UOC-S1 (Fig. 5) are consistent with spinel, we suspect that its range of condensation temperature and pressure conditions were probably similar to those inferred for the presumed solar spinel grain in Murray 2-19-13 described above.

The O isotopic composition of grain UOC-S2 indicates an origin in an AGB star of relatively low mass, but the grain's unusual ^{25}Mg enrichment is not predicted by models of such stars. Nittler et al. (2008) suggested that this grain originated in a star that was part of a binary system and experienced mass transfer from a more massive AGB stellar companion. The SAED patterns show that grain UOC-S2 is a single-crystal spinel that contains some minor stacking disorder, but EDS shows that it is otherwise stoichiometric and nearly pure Mg–Al spinel. Regarding the single-crystal nature and chemistry of UOC-S2, comparison with equilibrium predictions (Yoneda and Grossman, 1995; Ebel, 2006) suggests a condensation temperature between 1161 and 1221 K assuming a corresponding total gas pressures of 1×10^{-6} and 1×10^{-3} atm, respectively (see detailed discussion above for Murray 2-19-13).

The bright-field TEM images and SAED patterns acquired from the Fe-and Cr-rich grain ORG-36-21 reveal that it is polycrystalline and made up of three crystals (black arrowheads in Fig. 8). The angular spread among the [1 1 0] zone axis SAED patterns for the three grains is within 1.5° of one another (Fig. 8), showing that the grains occur in nearly identical orientations. Two explanations for the juxtaposition of the three grains are possible: either they condensed as three separate crystals and were mechanically brought together, or they condensed as a single assemblage under varied temperature and/or pressure conditions that resulted in a varied growth rate and direction. The first scenario seems unlikely because the mechanical attachment of three solid dust grains would not be expected to occur in an oriented fashion, but rather in three random orientations. We therefore infer that the second scenario is the more plausible explanation and that the oriented relationship, suggestive of epitaxy, resulted naturally from the time dependence of the condensation conditions within the circumstellar outflow. We note that the SEM image (Fig. 2b) of at least one other Orgueil grain of similar isotopic composition indicates a similar oriented growth mode.

Systematic variations in the composition of the ORG-36-21 spinel grains provide support for the idea of a single assemblage condensation scenario with time-dependent condensation parameters. The EDS data (Table 2) indicate that the Ti, Ni, and Al contents of the grains decreases from right to left, or respectively, from large grain to small, whereas Cr and Fe increase. As discussed above, Cr-rich spinels are thermodynamically predicted to condense at lower temperatures than Mg–Al spinels. Such predictions suggest that the right-most and largest grain (Fig. 8a, b) condensed first at the highest temperature. Growth of the middle and left-most domains would have initiated subsequently, at progressively lower temperatures. The systematic decrease in the grain sizes from right to left also suggests that the temperature of the ambient gas cycled, rather than decreased monotonically. Temperature cycling of the local gas due to changes in luminosity, for instance, may have affected the growth rates (e.g., Bernatowicz et al., 2005) to different degrees in different crystallographic orientations. The sub-grains, discussed in detail below, could have formed during the last cooling event.

The SAED patterns and HRTEM on the sub-grains in ORG-36-21 indicate structural coherency with the host spinel crystals in at least one orientation. Such coherency suggests that these regions share a genetic relationship with the host spinel. Given the different chemistries of the sub-regions and their structural relationship with the host spinels, we infer that these Ti-rich sub-grains formed by solid-state exsolution due to the decreasing solubility limit of Ti in Mg–Al spinel with decreasing grain temperature. If the sub-grains were inclusions, they likely would have been trapped inside the spinel crystals at random orientations and therefore would be unlikely to have any structural coherency with the bulk spinel. Moreover, inclusions would likely have significantly different chemistries than the host spinel. Although the precipitates have higher Ti and Al and lower Cr contents than the bulk spinel, they are nonetheless stoichiometric in composition. The rhombic morphology of the sub-grains, as revealed by the bright-field image (Fig. 9c), suggests that they had sufficient time to develop euhedral shapes with varied sizes. The variation in sub-grain size is probably not due to a difference in growth temperature, because it is unlikely that significant temperature gradients occurred across such small (micrometer sized) dust grains. Instead, we hypothesize that the exsolution, and hence, the size of the crystals, was diffusion limited. We note that some of the largest sub-grains occur near to or in the center of the crystals (with smaller grains nearer to the edge), where they would have been able to access supersaturated components within the full three-dimensional volume of the grain. In comparison, those at the edge had less volume from which to draw supersaturated components and thus crystallized into smaller grains.

As noted above for the other three presolar spinels reported herein, thermodynamic equilibrium calculations predict that pure $MgAl_2O_4$ will condense from cooling gas of

solar composition. At lower temperature (1221 K, 10^{-3} atm), Cr-rich spinel ($MgCr_2O_4$ = magnesiochromite), rather than chromite ($FeCr_2O_4$), is predicted to condense as the stable spinel phase (Yoneda and Grossman, 1995). Thermodynamically, the difficulty lies in getting Fe into the spinel phase because other materials, such as Fe metal, are competing for it (Lodders and Fegley, 1995). Ebel and Grossman (2000) showed theoretically that the protosolar disk could, in principle, condense Cr-rich, Fe-bearing spinel at different temperature intervals, but only by enriching the system in condensable elements. For example, for dust enrichments of 100× solar (where the abundances of condensable elements are increased by a factor of 100 relative to H and the solar composition, and the CI chondrite composition is taken to represent that of condensable solar system material), Cr-spinel can condense over a temperature range of 1600–1200 K with molar Fe/Mg and Cr/Al ratios that respectively range from 0.049 and 2.1 to 0.13 and 5.1 at a total pressure of 10^{-3} bar. At 1000× solar CI dust enrichment and total pressure of 10^{-3} bar, these calculations also predict formation of Cr-spinel with molar Fe/Mg and Cr/Al ratios that respectively range from 0.62 to 3.79 and 2.9 to 7.5 over a temperature interval of 1710–1260 K. In comparison, the molar Fe/Mg and Cr/Al ratios of ORG-36-21 range from 1.6 to 2.2 (ORG-36-21C and ORG-36-21L, respectively, Table 2) and 5.7 to 11.5 (ORG-36-21R and ORG-36-21L, respectively, Table 2).

Therefore, the mineral stoichiometry of ORG-36-21 either points to non-equilibrium condensation in its progenitor circumstellar envelope or equilibrium condensation from a gas that was highly enriched in condensable elements, relative to H and other extremely volatile elements. If the former case, then placing quantitative constraints on the condensation conditions of ORG-36-21 is not possible because kinetic models for spinel condensation are, to our knowledge, not available. We note that high Fe contents in some presolar silicate grains have led workers to invoke non-equilibrium condensation for those materials (Nguyen et al., 2007). If the latter case, then dust enrichments approaching 1000× solar appear to be required according to the calculations by Ebel and Grossman (2000). As condensation temperature decreases with decreases in dust enrichment (see Plate 10 of Ebel, 2006), then such calculations would predict that ORG-36-21 could have condensed over a temperature range of 1710–1260 K in order to reach the Fe contents as measured by EDS (Table 2). However, the O and Mg isotopic composition of ORG-36-21 (Table 1) indicates that it formed in a low-mass AGB or RGB star of approximately solar composition, and it is unclear how the outflowing envelope of such a star could become so enriched in condensable elements. The dust-enriched solar nebula condensation calculations (Ebel and Grossman, 2000) assume that prior to temperatures reaching a maximum, dust must be locally enhanced in the region under consideration. A subsequent increase in temperature causes vaporization of the dust and therefore localized enhancements of the oxygen fugacity (fO_2) relative to H and C compared to solar composition. In comparison, it seems highly unlikely that all the elements would condense in some region of the gaseous envelope around an RGB/AGB star, remain there, and then at some point later be completely vaporized by a temperature increase that would lead to enhanced fO_2. It is known that AGB stars will pulsate and that variations in luminosity could very well lead to periodic variations in effective temperatures and vaporization of dust (e.g., Bernatowicz et al., 2005). However, were such temperature cycling and vaporization to occur in the AGB envelope, it is unlikely to be CI (solar) like, but rather greatly enhanced in refractory materials. Whether refractory-enhanced gas could lead to condensation of chromite or Cr-rich spinel is unclear, but altogether, the evidence points more towards a non-equilibrium condensation origin for the grains in the ORG-36-21 assemblage rather than equilibrium condensation under dust-rich conditions.

4.3. Radiation processing

After their formation, presolar grains spent time both in the interstellar medium (ISM) and in the early solar nebula, and they are expected to have been exposed to radiation in both environments. It is thus worth exploring whether or not the spinel grains studied here show any sign of radiation processing, due to post-AGB irradiation (e.g., Verchovsky et al., 2004), cosmic rays in the ISM, or solar radiation in the early solar system prior to accretion into meteorite parent bodies. The primary mechanism for damage in ceramics in response to irradiation is the displacement of atoms from their preferred crystallographic positions, resulting in the formation of (Frenkel) pairs of vacancies and interstitials (Hobbs et al., 1994). Such displacement occurs as a result of either particle implantation and knock-on or radiation-induced electronic excitations (radiolysis). Which of the two processes dominates can depend on the energy of the incoming particle, its mass, the temperature of the crystal, its orientation, and its composition. Some defects can 'heal' after the implantation process through self-recombination. If such recovery is sufficiently rapid, the crystal can heal as quickly as it damages. If the recovery is inhibited, defects will accumulate resulting in damage that can range from, e.g., point-defect clusters (defect aggregation) to dislocation loops to complete amorphization of the crystal (McHargue, 1987).

The most obvious structural perturbation that we have observed in the presolar spinel grains is the disorder produced by stacking faults in the HRTEM images of the Group 2 (AGB) grain UOC-S2 (Fig. 7). The planar stacking fault on the right-hand side of UOC-S2 (Fig. 7a, b) is localized to a few tens of nanometers. Such stacking disorder, were it due to the aggregation of point defects as a result of cosmic-ray bombardment in the ISM, would not be expected to be localized because bombardment of the crystal would be isotropic, and given the potential grain lifetimes, occur over tens of millions of years (Jones, 2001). Therefore, we hypothesize that this stacking-fault disorder formed either as the result of slight perturbations to crystal growth during condensation in the circumstellar environment, or by impact-induced sheer strain as a response to grain-grain collisions, which could have occurred in the circumstellar environment, the ISM, or the solar nebula.

In comparison, the disorder near to the center of the grain that forms a loop with ½(1 1 1) displacement (Fig. 7a, e, f) is

interesting because Clinard et al. (1982) observed faulted dislocation loops on (1 1 0) and (1 1 1) planes of neutron-irradiated spinel at 925 K. Zinkle and Pells (1998) also observed defect nucleation predominantly on (1 1 1) planes in Ar^{+}-irradiated spinel at 4 MeV in experiments conducted at temperatures between 200 and 300 K. The conditions of these experiments do not necessarily match those expected for the ISM, which is dominated by protons and alpha particles accelerated at hundreds of MeV to GeV levels and higher (Simpson, 1983; Beatty and Westerhoff, 2009) and grain temperatures of approximately 10–50 K (Draine, 2003; Draine and Hensley, 2013). Thus, while the above experiments indicate that spinel will indeed damage in response to irradiation, it seems unlikely that the stacking disorder we observe in UOC-S2 was due to defect nucleation on (1 1 1) planes as a result of interstellar radiation processing. An alternative possibility is that ½(1 1 1) displacement either formed during condensation as a result of perturbations to nucleation or, as with the stacking fault on the right-hand side of UOC-S2, formed as a result of grain-grain collisions. For Mg–Al spinel, the most commonly observed slip planes are (1 1 0) and (1 1 1) (Mitchell, 1999), and nanoindentation experiments on synthetic spinel have revealed that it plastically deforms via slip bands on (1 1 1) planes (Lloyd et al., 2002). It is conceivable that grain-grain collisions in the circumstellar envelope, the ISM, or the solar nebula could have produced the observed stacking disorder near the center of the grain as well.

It has been shown that irradiation can produce a metastable spinel phase in the transition from the crystalline to amorphous state. For example, Yu et al. (1994) compared the convergent-beam electron-diffraction patterns obtained from undamaged spinel to those acquired from spinel damaged by 400 keV Xe^{2+} at 100 K, and found a marked reduction in the intensity of the (2 2 0) reflection of the latter. They suggested that the transformation to a metastable state with a smaller cubic unit cell would lead to the systematic absence of <2 2 0> reflections in a diffraction pattern acquired down the [0 0 1] zone axis. A slight weakening of the (2 2 0) reflections in spinel irradiated with 4 MeV Ar^{+} at 200–300 K was also observed by Zinkle and Pells (1998), although they concluded that the metastable phase transition did not occur for the irradiation conditions used in their samples. While we do not find systematic absences in reflections from the SAED patterns acquired from the presolar spinel samples, we do observe small intensity variations in the reflections of some of the [1 1 0] zone-axis patterns acquired across the UOC-S2 grain (cf., Fig. 6c–e). Specifically, the intensity of <2 2 0> and <0 0 2> type reflections vary in the SAED pattern acquired from the center of the crystal, whereas those and <1 1 1> type reflections show varied intensity in the SAED pattern acquired from the left-hand side of the grain. Although all of the SAED patterns were acquired at the same goniometer tilt angle, we simulated SAED patterns (not shown) to test whether differences in crystal orientation, as a result of changes in growth during condensation (e.g., Zega et al., 2011), could produce the variations that we observe. Our simulations indicate that subtle changes in orientation ($\leqslant 2°$) can reproduce intensity variations in the reflections of [1 1 0] patterns. Such a spread in crystal orientation might result from changes in growth direction during condensation (e.g., Zega et al., 2011), by impact processing in the ISM, or during accretion into the meteorite parent body. Furthermore, the diffractograms (Fig. 7c, d) obtained from the HRTEM images indicate strong <2 2 0> -type ordering, arguing against the formation of metastable forms of spinel.

4.4. Relevance to IR astronomy

Infrared spectroscopy of O-rich AGB stars has revealed a 13-μm emission feature that has been attributed to several phases, including α-Al_2O_3, α-Al_2O_3 mantled by silicate material, SiO_2 and other polymerized silicates, and Mg–Al spinel (Onaka et al., 1989; Kozasa and Sogawa, 1997; Posch et al., 1999; Speck et al., 2000). Polycylcic aromatic hydrocarbons (PAHs) have also been suggested, but it seems less likely that such compounds might explain a 13-μm emission feature in the kinds of O-rich stars from which the spinels we report on here were derived (although see Acke et al., 2013). Nonetheless, while the data that we report here do not directly address the controversy over the identification of this emission feature, they do show that O-rich AGB stars can condense crystalline spinel grains. Moreover, the range in solid-solution chemistry of the presolar spinel grains reported herein could affect their IR emission, and such chemistry might need to be taken into account for future work aimed at modeling remotely sensed IR spectra of O-rich RGB and AGB stars.

5. SUMMARY AND CONCLUSIONS

We report here the first identification of presolar Fe- and Cr-rich spinel grains in a primitive meteorite. Microstructural and crystal-chemical data for one of these grains, as well as for three presolar Mg–Al-rich spinel grains, indicate that all are crystalline and are consistent with spinel lattice parameters (S. G. Fd3m, $0.810\ \text{nm} < a_0 < 0.854\ \text{nm}$). All four grains have isotopic signatures indicating an origin in low-mass AGB stars. The three Mg–Al grains are single-crystal spinel, whereas the Fe–Cr-rich assemblage is polycrystalline, consisting of three grains with <1.5° spread in crystallographic orientation. The three grains contain multiple <100 nm sub-grains. We infer that the grains condensed sequentially in the circumstellar envelope under fluctuating temperature conditions. The structural coherency of the sub-grains with their host spinel, but their different chemistry compared to their host, suggests that they are precipitates rather than inclusions.

None of the four grains are pure $MgAl_2O_4$. All contain Cr and Fe, and some also contain variable amounts of Ti, Ni, and minor Si. Three grains conform to spinel stoichiometry (i.e., XY_2O_4, where X and Y are cations such as Mg and Al, respectively), whereas UOC-S1 is deficient in Mg. Comparison of the grain data to predictions by equilibrium thermodynamics constrains the temperature of condensation between 1221 and 1500 K for UOC-S2 and 1161 and 1221 K for Murray 2-19-13, assuming a total gas pressure of, respectively, 10^{-6} and 10^{-3} atm. The microstructural and crystal chemical data on the other two grains (ORG-36-21 and UOC-S1) are inconsistent with equilibrium

predictions, and thus constraining condensation conditions for them is not possible without detailed kinetic models.

One grain (UOC-S2) contains evidence of localized (1 1 1) stacking disorder. Such disorder is similar to effects described for synthetic spinel grains irradiated under laboratory conditions (e.g., Clinard et al., 1982; McHargue, 1987; Zinkle and Pells, 1998). However, given that irradiation of oxide grains in the ISM was likely isotropic, a more abundant and uniformly distributed array of structural perturbations is expected. That (1 1 1) planes are commonly observed slip planes in Mg–Al spinel (Mitchell, 1999) and nanoindentation experiments on synthetic spinel show that it plastically deforms via slip bands on (1 1 1) planes (Lloyd et al., 2002) would appear to favor stacking-fault formation via grain–grain collision, either in the circumstellar envelope, the ISM, or the solar nebula for presolar spinel grain UOC-S2.

Detailed analysis of such presolar spinel stardust offers a way of doing astronomy in the laboratory. The data that we present here unequivocally demonstrate that low-mass O-rich RGB/AGB stars condense crystalline and stoichiometric spinel grains. However, the non-stoichiometric composition of UOC-S1 and the Fe–Cr-rich composition of ORG-36-21 indicate that non-equilibrium processes were at work in their condensation environments. Moreover, the deviation from pure end-member $MgAl_2O_4$ for all of the presolar spinel grains measured herein suggests that a range of spinel compositions should be considered in developing reference libraries used for the modeling of IR spectra obtained from circumstellar dust shells or proto-planetary nebulae.

ACKNOWLEDGEMENTS

This research was supported by the NASA Cosmochemistry Program (grants NNH09AL20I to RMS, NNX10AI63G to LRN, NNX11AH14G to EZ, and NNX12AK47G to TJZ) and a Carnegie Institution of Washington Fellowship to F. Gyngard. We thank AE Dimitri Papanastassiou and three anonymous reviewers for constructive comments which helped improve the paper.

REFERENCES

Acke B., Degroote P., Lombaert R., de Vries B. L., Smolders K., Verhoelst T., Lagadec E., Gielen C., Van Winckel H. and Waelkens C. (2013) Amorphous carbon in the disk around the post-AGB binary HR 4049. Discerning dust species with featureless opacity curves. *Astron. Astrophys.* **551**, A76–A91.

Alexander C.M.O'D. (1993) Presolar SiC in chondrites: How variable and how many sources? *Geochim. Cosmochim. Acta* **57**, 2869–2888.

Amari S., Anders E., Virag A. and Zinner E. (1990) Interstellar graphite in meteorites. *Nature* **345**, 238–240.

Beatty J. J. and Westerhoff S. (2009) The highest-energy cosmic rays. *Annu. Rev. Nucl. Part. Sci.* **59**, 319–345.

Bernatowicz T., Fraundorf G., Tang M., Anders E., Wopenka B., Zinner E. and Fraundorf P. (1987) Evidence for interstellar SiC in the Murray carbonaceous meteorite. *Nature* **330**, 728–730.

Bernatowicz T. J., Wali Akande O., Croat T. K. and Cowsik R. (2005) Constraints on grain formation around carbon stars from laboratory studies of presolar graphite. *Astrophys. J.* **631**, 988–1000.

Boothroyd A. I. and Sackmann I.-J. (1999) The CNO-isotopes: deep circulation in red giants and first and second dredge-up. *Astrophys. J.* **510**, 232–250.

Brearley A. J. and Jones R. H. (1998) Chondritic meteorites. In *Planetary Materials* (ed. J. J. Papike). Mineralogical Society of America, Washington DC, p. 398.

Choi B. G., Huss G. R., Wasserburg G. J. and Gallino R. (1998) Presolar corundum and spinel in ordinary chondrites: origins from AGB stars and a supernova. *Science* **282**, 1284–1289.

Clinard F. W. J., Hurley G. F. and Hobbs L. W. (1982) Neutron irradiation damage in MgO, Al_2O_3, and $MgAl_2O_4$ ceramics. *J. Nucl. Mater.* **108 & 109**, 655–670.

Croat T. K., Stadermann F. J. and Bernatowicz T. J. (2005) Presolar graphite from AGB stars: microstructure and s-process enrichment. *Astrophys. J.* **631**, 976–987.

Daulton T. L., Bernatowicz T. J., Lewis R. S., Messenger S., Stadermann F. J. and Amari S. (2002) Polytype distribution in circumstellar silicon carbide. *Science* **296**, 1852–1855.

Dauphas N., Remusat L., Chen J. H., Roskosz M., Papanastassiou D. A., Stodolna J., Guan Y. B., Ma C. and Eiler J. M. (2010) Neutron-rich chromium isotope anomalies in supernova nanoparticles. *Astrophys. J.* **720**, 1577–1591.

Dearborn D. S. P. (1992) Diagnostics of stellar evolution: The oxygen isotopes. *Phys. Rep.* **210**, 367–382.

Deer W. A., Howie R. A. and Zussman J. (1992) *An Introduction to the Rock-Forming Minerals*. Longman Group Ltd., Essex, UK, p. 696.

Draine B. T. (2003) Interstellar dust grains. *Annu. Rev. Astron. Astrophys.* **41**, 241–289.

Draine B. T. and Hensely B. (2013) Magnetic nanoparticles in the interstellar medium: Emission spectrum and polarization. *Astrophys. J.* **765**, 159–182.

Ebel D. S. (2006) Condensation of rocky material in astrophysical environments. In *Meteorites and the Early Solar System II* (eds. D. S. Lauretta and H. Y. McSween, Jr.). University of Arizona Press, Tucson. pp. 253–277.

Ebel D. S. and Grossman L. (2000) Condensation in dust-enriched systems. *Geochim. Cosmochim. Acta* **64**, 339–366.

Graham G. A., Teslich N. E., Kearsley A. T., Stadermann F. J., Stroud R. M., Dai Z. R., Ishii H. A., Hutcheon I. D., Bajt S., Snead C. J., Weber P. K. and Bradley J. P. (2008) Applied focused ion beam techniques for sample preparation of astromaterials for integrated nanoanalysis. *Meteorit. Planet. Sci.* **43**, 561–569.

Gyngard F., Zinner E., Nittler L. R., Morgand A., Stadermann F. J. and Hynes K. M. (2010) Automated NanoSIMS measurements of spinel stardust from the Murray meteorite. *Astrophys. J.* **717**, 107–120.

Heaney P. J., Vicenzi E. P., Gianuzzi L. A. and Livi K. J. T. (2001) Focused ion beam milling: A method of site-specific sample preparation for microanalysis of Earth and planetary materials. *Am. Mineral.* **86**, 1094–1099.

Hobbs L. W., Clinard F. W. J., Zinkle S. J. and Ewing R. C. (1994) Radiation effects in ceramics. *J. Nucl. Mater.* **216**, 291–321.

Hovmöller S. (1992) CRISP – crystallographic image-processing on a personal-computer. *Ultramicroscopy* **41**, 121–135.

Hynes K. M. and Gyngard F. (2009) The presolar grain database. *Lunar Planet. Sci. Conference*. #1198 (abstr.).

Hynes K. M., Croat T. K., Amari S., Mertz A. F. and Bernatowicz T. J. (2010) Structural and isotopic microanalysis of presolar SiC from supernovae. *Meteorit. Planet. Sci.* **45**, 596–614.

Jones A. P. (2001) Interstellar and circumstellar grain formation and survival. *Philos. Trans. R. Soc. A Math. Phys. Eng. Sci.* **359**, 1961–1972.

Kozasa T. and Sogawa H. (1997) Formation of dust grains in circumstellar envelopes of oxygen-rich AGB stars. *Astrophys. Space Sci.* **251**, 165–170.

Lee M. R., Bland P. A. and Graham G. (2003) Preparation of TEM samples by focused ion beam (FIB) techniques: applications to the study of clays and phyllosilicates in meteorites. *Mineral. Mag.* **67**, 581–592.

Leitner J., Vollmer C., Hoppe P. and Zipfel J. (2012) Characterization of presolar material in the CR chondrite Northwest Africa 852. *Astrophys. J.* **745**, 38–54.

Lloyd S. J., Aldareguia-Molina J. M. and Clegg W. J. (2002) Deformation under nanoindents in sapphire, spinel and magnesia examined using transmission electron microscopy. *Philos. Mag. A* **82**, 1963–1969.

Lodders K. (2003) Solar system abundances and condensation temperatures of the elements. *Astrophys. J.* **591**, 1220–1247.

Lodders K. and Fegley, Jr., B. (1995) The origin of circumstellar silicon carbide grains found in meteorites. *Meteoritics* **30**, 661–678.

MacPherson G. J. (2004) Calcium-aluminum-rich inclusions in chondritic meteorites. In *Meteorites, Comets, and Planets* (ed. A. M. Davis) *Vol. 1 Treatise on Geochemistry* (eds. H. D. Holland and K. K. Turekian). Elsevier-Pergamon, Oxford.pp. 201–246.

MacPherson G. J. and Grossman L. (1984) 'Fluffy' type A Ca-, Al-rich inclusions in the Allende meteorite. *Geochim. Cosmochim. Acta* **48**, 29–46.

McHargue C. (1987) The mechanical and tribological properties of ion implanted ceramics. In *Ion Beam Modification of Insulators* (eds. P. Mazzoldi and G. Arnold). Elsevier, Amsterdam, pp. 223–243.

Mitchell T. E. (1999) Dislocations and mechanical properties of $MgO–Al_2O_3$ spinel single crystals. *J. Am. Ceram. Soc.* **82**, 3305–3316.

Nguyen A. N., Stadermann F. J., Zinner E., Stroud R. M., Alexander C.M.O'D. and Nittler L. R. (2007) Characterization of presolar silicate and oxide grains in primitive carbonaceous chondrites. *Astrophys. J.* **656**, 1223–1240.

Nguyen A., Nittler L. R., Stadermann F. J., Stroud R. M. and Alexander C.M.O'D. (2010) Coordinated analyses of presolar grains in the Allan Hills 77307 and Queen Elizabeth range 99177 meteorites. *Astrophys. J.* **719**, 166–189.

Nittler L. R., Alexander C.M.O'D., Gao X., Walker R. M. and Zinner E. (1997) Stellar sapphires: The properties and origins of presolar Al_2O_3 in meteorites. *Astrophys. J.* **483**, 475–495.

Nittler L. R. and Alexander C.M.O'D. (2003) Automated isotopic measurements of micron-sized dust: application to meteoritic presolar silicon carbide. *Geochim. Cosmochim. Acta* **67**, 4961–4980.

Nittler L. R., Alexander C.M.O'D., Gao X., Walker R. M. and Zinner E. K. (1994) Interstellar oxide grains from the Tieschitz ordinary chondrite. *Nature* **370**, 443–446.

Nittler L. R., Alexander C.M.O'D., Stadermann F. J. and Zinner E. K. (2005) Presolar chromite in Orgueil. *Meteorit. Planet. Sci.* **40**(Suppl.), A114 (abstr.).

Nittler L. R., Alexander C.M.O'D., Gallino R., Hoppe P., Nguyen A., Stadermann F. and Zinner E. K. (2008) Aluminum-, calcium- and titanium rich oxide stardust in ordinary chondrite meteorites. *Astrophys. J.* **682**, 1450–1478.

Nittler L. R., Gyngard F. and Zinner E. (2010) Extreme O isotopic anomalies in presolar oxides from the Murray CM2 chondrite. *Meteorit. Planet. Sci.* **45**, A153.

Nollet K. M., Busso M. and Wasserburg G. J. (2003) Cool bottom processes on the thermally pulsing asymptotic giant branch and the isotopic composition of circumstellar dust grains. *Astrophys. J.* **582**, 1036–1058.

Onaka T., de Jong T. and Willems F. J. (1989) A study of M Mira variables based on IRAS LRS observations. I – Dust formation in the circumstellar shell. *Astron. Astrophys.* **218**, 169–179.

Palmerini S., La Cognata M., Cristallo S. and Busso M. (2011) Deep mixing in evolved stars. I. The effect of reaction rate revisions from C to Al. *Astrophys. J.* **729**, 1–21.

Papike J. J. (1998) Planetary materials. In *Reviews in Mineralogy* (ed. P. H. Ribbe). Mineralogical Society of America, Washington DC.

Posch T., Kerschbaum F., Mutschke H., Fabian D., Dorschner J. and Hron J. (1999) On the origin of the 13 μm feature. A study of ISO-SWS spectra of oxygen-rich AGB stars. *Astron. Astrophys.* **352**, 609–618.

Qin L. P., Carlson R. W. and Alexander C.M.O'D. (2011) Correlated nucleosynthetic isotopic variability in Cr, Sr, Ba, Sm, Nd and Hf in Murchison and QUE 97008. *Geochim. Cosmochim. Acta* **75**, 7806–7828.

Simpson J. A. (1983) Elemental and isotopic composition of the galactic cosmic rays. *Annu. Rev. Nucl. Part. Sci.* **33**, 323–381.

Speck A. K., Barlow M. J., Sylvester R. J. and Hofmeister A. M. (2000) Dust features in the 10-μm infrared spectra of oxygen-rich evolved stars. *Astron. Astrophys. Suppl. Ser.* **146**, 437–464.

Stadelmann P. A. (1987) EMS – A software package for electron-diffraction analysis and HREM image simulation in materials science. *Ultramicroscopy* **21**, 131–145.

Stadermann F. J., Croat T. K., Bernatowicz T. J., Amari S., Messenger S., Walker R. M. and Zinner E. (2005) Supernova graphite in the NanoSIMS: Carbon, oxygen and titanium isotopic compositions of a spherule and its TiC sub-components. *Geochim. Cosmochim. Acta* **69**, 177–188.

Stroud R. M., Alexander C.M.O'D. and MacPherson G. J. (2000) A precise new method of microsampling chondritic material for transmission electron microscopy analysis: preliminary application to calcium-aluminum-rich inclusions and associated matrix material in the Vigarano CV3 meteorite. *Meteorit. Planet. Sci.* **35**, A153 (abstr.).

Stroud R. M., Nittler L. R. and Alexander C.M.O'D. (2004) Polymorphism in presolar Al_2O_3 grains from asymptotic giant branch stars. *Science* **305**, 1455–1457.

Stroud R. M., Nittler L. R. and Alexander C.M.O'D. (2006) Supernova nierite (α-Si_3N_4) from Murchison. *Meteorit. Planet. Sci.* **41**, A168 (abstr.).

Stroud R.M., Nittler L.R., Alexander C.M.O'D., Zinner E. (2007) Transmission electron microscopy and secondary ion mass spectrometry of an unusual Mg-rich presolar Al_2O_3 grain. *Lunar Planet. Sci. Conference XXXVIII*. 2203 (abstr.).

Stroud R.M., Floss C., Stadermann F.J. (2009) Structure, elemental composition, and isotopic composition of presolar silicates in MET 00426. *Lunar Planet. Sci. Conference XL*, 1063 (abstr.).

Verchovsky A. B., Wright I. P. and Pillinger C. T. (2004) Astrophysical significance of asymptotic giant branch stellar wind energies recorded in meteoritic SiC grains. *Astrophys. J.* **607**, 611–619.

Vollmer C., Hoppe P., Brenker F. E. and Holzapfel C. (2007) Stellar $MgSiO_3$ perovskite: A shock-transformed stardust silicate found in a meteorite. *Astrophys. J.* **666**, L49–L52.

Vollmer C., Brenker F. E., Hoppe P. and Stroud R. M. (2009) Direct laboratory analysis of silicate stardust from red giant stars. *Astrophys. J.* **700**, 774–782.

Wasserburg G. J., Boothroyd A. I. and Sackmann I.-J. (1995) Deep circulation in red giant stars: A solution to the carbon and oxygen isotope puzzles? *Astrophys. J. Lett.* **447**, L37–L40.

Yoneda S. and Grossman L. (1995) Condensation of $CaO–MgO–Al_2O_3–SiO_2$ liquids from cosmic gases. *Geochim. Cosmochim. Acta* **59**, 3413–3444.

Yu N., Sickafus K. E. and Nastasi M. (1994) First observation of amorphization in single-crystal $MgAl_2O_4$ spinel. *Philos. Mag. Lett.* **70**, 235–240.

Zega T. J., Hanbicki A. T., Erwin S. C., Zutic I., Kioseoglou G., Li C. H., Jonker B. T. and Stroud R. M. (2006) Determination of interface atomic structure and its impact on spin transport using Z-contrast microscopy and density-functional theory. *Phys. Rev. Lett.* **96**, 196101.

Zega T. J., Nittler L. R., Busemann H., Hoppe P. and Stroud R. M. (2007) Coordinated isotopic and mineralogic analyses of planetary materials enabled by in situ lift-out with a focused ion beam scanning electron microscope. *Meteorit. Planet. Sci.* **42**, 1373–1386.

Zega T. J., Alexander C.M.O'D., Nittler L. R. and Stroud R. M. (2011) A transmission electron microscopy study of presolar hibonite. *Astrophys. J.* **730**, 83–93.

Zinkle S. J. and Pells G. P. (1998) Microstructure of Al_2O_3 and $MgAl_2O_4$ irradiated at low temperatures. *J. Nucl. Mater.* **253**, 120–132.

Zinner E. K. (2004) Presolar Grains. In *Meteorites, Comets, and Planets* (ed. A. M. Davis) *Vol. 1 Treatise on Geochemistry* (eds. H. D. Holland and K. K. Turekian). Elsevier-Pergamon, Oxford. pp. 17–39.

Zinner E., Amari S., Guinness R., Nguyen A., Stadermann F. J., Walker R. M. and Lewis R. (2003) Presolar spinel grains from the Murray and Murchison carbonaceous chondrites. *Geochim. Cosmochim. Acta* **67**, 5083–5095.

Zinner E., Nittler L. R., Hoppe P., Gallino R., Straniero O. and Alexander C.M.O'D. (2005) Oxygen, magnesium and chromium isotopic ratios of presolar spinel grains. *Geochim. Cosmochim. Acta* **69**, 4149–4165.

Associate editor: Dimitri A. Papanastassiou